AFRL-AFOSR-UK-TR-2022-0029

Hypersonic Acoustic Loading (HAL)

Drikakis, Dimitris
RESEARCH FOUNDATION P.L LIMITED
66 Metochiou
Egkomi Nicosias, Nicosia, , 2407
CY

03/07/2024
Final Technical Report

DISTRIBUTION A: Distribution approved for public release.

Air Force Research Laboratory
Air Force Office of Scientific Research
European Office of Aerospace Research and Development
Unit 4515 Box 14, APO AE 09421

REPORT DOCUMENTATION PAGE

PLEASE DO NOT RETURN YOUR FORM TO THE ABOVE ORGANIZATION.

1. REPORT DATE 20240307	**2. REPORT TYPE** Final	**3. DATES COVERED** **START DATE** 20190515	**END DATE** 20240114

4. TITLE AND SUBTITLE
Hypersonic Acoustic Loading (HAL)

5a. CONTRACT NUMBER	**5b. GRANT NUMBER** FA9550-19-1-7018	**5c. PROGRAM ELEMENT NUMBER**
5d. PROJECT NUMBER	**5e. TASK NUMBER**	**5f. WORK UNIT NUMBER**

6. AUTHOR(S)
Dimitris Drikakis

7. PERFORMING ORGANIZATION NAME(S) AND ADDRESS(ES)
RESEARCH FOUNDATION P.L LIMITED
66 Metochiou
Egkomi Nicosias, Nicosia 2407
CY

8. PERFORMING ORGANIZATION REPORT NUMBER

9. SPONSORING/MONITORING AGENCY NAME(S) AND ADDRESS(ES) EOARD UNIT 4515 APO AE 09421-4515	**10. SPONSOR/MONITOR'S ACRONYM(S)** AFRL/AFOSR IOE	**11. SPONSOR/MONITOR'S REPORT NUMBER(S)** AFRL-AFOSR-UK-TR-2022-0029

12. DISTRIBUTION/AVAILABILITY STATEMENT
A Distribution Unlimited: PB Public Release

13. SUPPLEMENTARY NOTES

14. ABSTRACT

The work comprised high-resolution direct numerical simulations (DNS) and implicit large eddy simulations (ILES) for high-speed flows and acoustics featuring shock-boundary layer interaction (SBLI). The cases concerned hypersonic flow over a flat panel, SBLI over a compression ramp, and SBLI for the RC-19 tunnel. The SBLI cases included statistically- and dynamically-deformed cases. An assessment of computational requirements for performing high-resolution simulations was also performed. The findings improved our understanding of SBLI, the acoustic near-wall effects, and the role of vorticity in such flows. Furthermore, the research provided insight into the best computational practices for achieving high accuracy in such flows. Finally, the data produced from this award will be used in the future to develop and apply machine learning models and provide insight into the coupling of computational fluid dynamics and structural mechanics methods.

15. SUBJECT TERMS

16. SECURITY CLASSIFICATION OF:			**17. LIMITATION OF ABSTRACT** SAR	**18. NUMBER OF PAGES** 34
a. REPORT U	**b. ABSTRACT** U	**c. THIS PAGE** U		

19a. NAME OF RESPONSIBLE PERSON DAVID SWANSON	**19b. PHONE NUMBER** *(Include area code)* 785-6565

Standard Form 298 (Rev.5/2020)
Prescribed by ANSI Std. Z39.18

Final Report- Award FA9550-19-1-7018

Dimitris Drikakis[1] and Ioannis W. Kokkinakis[1]
University of Nicosia, Nicosia, CY-2417, Cyprus[a)]

This is the final report summarising the key findings of the project. The work comprised high-resolution direct numerical simulations (DNS) and implicit large eddy simulations (ILES) for high-speed flows and acoustics featuring shock-boundary layer interaction (SBLI). The cases concerned hypersonic flow over a flat panel, SBLI over a compression ramp, and SBLI for the RC-19 tunnel. The SBLI cases included statistically- and dynamically-deformed cases. An assessment of computational requirements for performing high-resolution simulations was also performed. The findings improved our understanding of SBLI, the acoustic near-wall effects, and the role of vorticity in such flows. Furthermore, the research provided insight into the best computational practices for achieving high accuracy in such flows. Finally, the data produced from this award will be used in the future to develop and apply machine learning models and provide insight into the coupling of computational fluid dynamics and structural mechanics methods.

I. INTRODUCTION

Shock-wave boundary layer interaction (SBLI) occurs at high-speed flows, particularly when a surface protrudes abruptly towards the flow, e.g., a deflected flap or an inlet ramp. Furthermore, SBLI features flow separation and reattachment, low-frequency unsteadiness, and high local thermal loads. All of the above influence the performance of supersonic aircraft; thus, the interest in studying SBLI[1–8]. In addition, under supersonic conditions, flight objects are subjected to acoustic fatigue due to pressure fluctuations beneath the turbulent boundary layers (TBLs)[1,5,9,10]. The physical mechanism behind the low-frequency SBLI unsteadiness remains elusive and is widely debated Clemens and Narayanaswamy [11].

Surface deformations caused by shock-boundary layer interaction (SBLI) can lead to a loss of efficiency of the aerodynamic surfaces and unwanted wall pressure fluctuations, possibly leading to structural vibrations[12]. The above can significantly influence aerostructures' overall aerodynamic and structural integrity at high speeds. SBLI over non-deformed planar surfaces has been extensively studied in the past both experimentally[1,13–19] and numerically[3–5,20–33].

Interest in the examination of SBLI for deformed buckled panel surfaces, however, has gained more attention in the last decade, both experimentally[11,34–49] and numerically[50–59]. High-speed flights exhibit extreme aerothermodynamic loads, which affect the lightweight structures, thus resulting in strong, dynamic fluid–structure coupling. Therefore, understanding SBLI under surface deformation will increase the predictive and design capabilities.

Direct numerical simulation (DNS) resolves the turbulent flow's relevant physical spatial and temporal scales. As a result, it is and will be prohibitively expensive in the foreseeable future for most practical flows and regimes of interest at moderate-to-high Reynolds numbers. Reynolds-averaged Navier–Stokes (RANS) approaches focus on statistical moments for an ensemble of realizations and try to model the effects of the turbulence. Small-scale turbulent flow dynamics are widely viewed as universal, resulting from a cascade process from the breakdown of larger scales originating to the integral scales.

In a coarse-grained simulation (CGS), large energy-containing structures are resolved, smaller structures are spatially filtered out, whereas unresolved subgrid-scale (SGS) effects are modeled[60]. CGS includes classical large eddy simulation (LES) strategies employing an explicit SGS model or implicit LES (ILES) relying on SGS modeling and filtering provided by physics-capturing numerical algorithms, i.e., shock-capturing schemes typically employed in finite volume methods. Understanding of this so-called spectral gap, or scale separation, between the large (integral) and the small (viscous) turbulence scales has further improved over the last decade, particularly about CGS modeling[61]. The CGS strategy of separating the resolved from the unresolved scales and modeling the physics effects of the latter constitutes a viable intermediate approach between DNS and RANS to address practical geometries and multiphysics.

In the present work, we considered different statically and dynamically buckled rectangular panel surface shapes, which adhere to several basic modes commonly encountered in fluid–structure interaction (FSI) and their effect on the TBL and SBLI. By doing so, the problem is simplified by decoupling it into a geometrically simpler variant that isolates some of the crucial effects of the surface deformations on the TBL and SBLI response, thus enabling a better understanding of fully coupled FSI, such as those being performed experimentally in the RC-19 wind tunnel set-up[39,44].

Small deflection angles of the shock generator wedge ($\theta <$ 12 deg) have been successfully modeled computationally[44,45]. However, though the aeroelastic framework captures the onset of the dynamic instability for the 12-degree wedge case, it incorrectly predicts the modal and frequency content of the post-flutter response. These errors are attributed to the omission of unsteady interactions in the quasi-steady enriched piston theory model. For the 12 deg case, experiments[44] reveal shock-induced limit cycle oscillations (LCO) near the region of shock-induced separation. In this case, the dynamic panel response exhibited frequencies on the order of the SBLI-induced low-frequency unsteadiness, highlighting the potential for coupling between the thin panel and shock impingement. Nevertheless, the simplified models can predict flutter onset for attached and separated SBLI. While the post-flutter response is captured for attached flows, improvements to the

---

[a)] Electronic mail: drikakis.d@unic.ac.cy.

fluid model are required to obtain the correct limit-cycle behavior in shock-induced separation. This includes developing and implementing models that capture low-frequency shock oscillations and unsteady interactions between the surface motion and separation bubble.

To address the above limitations, we have employed shock-capturing, high-order schemes with nominal accuracy up to 11th-order, which has previously been used in similar simulations of compressible turbulent boundary layers (TBL)[6,9,62,63] and shock wave TBL interaction (SBLI)[5,64,65], amongst other flows.

This final report summarises the work carried out during the project. Further technical details can be found in the journal publications[5,10,66–68].

II. COMPUTATIONAL METHODOLOGY

A. Governing equations

The compressible Navier-Stokes equations (NSE) are solved using the finite volume method (FVM) for an ideal gas. In integral form, the NSEs are formulated as follows:

$$\frac{\partial}{\partial t}\iiint\limits_V \rho \,\mathrm{dV} = -\oint\!\!\!\oint\limits_A \rho\,(\mathbf{u}\cdot\hat{\mathbf{n}})\,\mathrm{dA} \tag{1}$$

$$\begin{aligned}\frac{\partial}{\partial t}\iiint\limits_V \rho\mathbf{u}\,\mathrm{dV} = &-\oint\!\!\!\oint\limits_A \rho\,\mathbf{u}\,(\mathbf{u}\cdot\hat{\mathbf{n}})\,\mathrm{dA} - \oint\!\!\!\oint\limits_A p\,\hat{\mathbf{n}}\,\mathrm{dA}\\ &+\oint\!\!\!\oint\limits_A (\tau\cdot\hat{\mathbf{n}})\,\mathrm{dA}\end{aligned} \tag{2}$$

$$\begin{aligned}\frac{\partial}{\partial t}\iiint\limits_V \rho e\,\mathrm{dV} = &-\oint\!\!\!\oint\limits_A \rho\,(\mathbf{u}\cdot\hat{\mathbf{n}})\,e\,\mathrm{dA} - \oint\!\!\!\oint\limits_A p\,(\mathbf{u}\cdot\hat{\mathbf{n}})\,\mathrm{dA}\\ &+\oint\!\!\!\oint\limits_A (\mathbf{u}\cdot\tau)\cdot\hat{\mathbf{n}}\,\mathrm{dA} - \oint\!\!\!\oint\limits_A (\mathbf{q}\cdot\hat{\mathbf{n}})\,\mathrm{dA}\end{aligned} \tag{3}$$

where ρ is the density; $\mathbf{u}$ is the velocity vector; p is the static pressure; $\hat{\mathbf{n}}$ is the outward pointing unit normal of surface element dA of the closed finite control volume dV; e is the total energy per unit mass given by $e = i + \mathbf{u}\cdot\mathbf{u}/2$; i is the specific internal energy, which for a calorically perfect gas is given by:

$$i = c_v T = \frac{p}{\rho\,(\gamma-1)}$$

T is the temperature, c_v is the specific heat capacity at constant volume, and γ is the heat capacity ratio (or adiabatic index) defined as $\gamma = c_p/c_v$ where c_p is the specific heat capacity at constant pressure and $R_s = c_p - c_v = c_v\,(\gamma-1)$ is the specific gas constant.

For a Newtonian fluid, the shear stress tensor is given by:

$$\tau = \lambda_b\,(\nabla\cdot\mathbf{u})\,\mathsf{I} + \mu\left[\nabla\mathbf{u} + (\nabla\mathbf{u})^T\right]$$

where I is the identity tensor; the bulk viscosity is given by $\lambda_b = -2\mu/3$ according to Stokes' hypothesis; and μ is the dynamic viscosity obtained by Sutherland's Law as:

$$\mu(T) = \mu_{ref}\left(\frac{T}{T_{ref}}\right)^{\frac{3}{2}}\frac{T_{ref}+T_s}{T+T_s} \tag{4}$$

where the free-stream values are used as the reference and the Sutherland temperature is $T_s = 110.4$K.

Fourier's Law of heat conduction calculates the heat flux:

$$\mathbf{q} = -\kappa\nabla T$$

where κ is the heat conductivity given by:

$$\kappa(T) = \frac{c_p}{\mathrm{Pr}}\mu(T)$$

and $\mathrm{Pr} = 0.72$ is Prandtl's number.

B. Numerical methods

We employ the block-structured grid code CNS3D that solves the Navier–Stokes equations using the finite-volume method (FVM). The advective terms are solved using the Godunov-type (upwind) method, whose inter-cell numerical fluxes are calculated by solving the Riemann problem using the reconstructed values of the primitive variables at the cell interfaces. A one-dimensional swept unidirectional stencil is used for the spatial reconstruction. Two different slope limiting approaches have been implemented in conjunction with the approximate HLLC Riemann solver, namely the: (i) Monotone upstream-centred schemes for conservation laws (MUSCL) and (ii) Weighted essentially non-oscillatory (WENO). In particular, the following slope-limiters are examined:

- MUSCL 2nd order Monotonized Central (M2)[69];
- MUSCL 5th (M5) order[70];
- WENO 9th (W9) order[71].

Finally, we use a second-order central scheme for the viscous terms. The solution is advanced in time using a five-stage (fourth-order accurate) optimal strong-stability-preserving Runge–Kutta method[72]. Further details of the numerical aspects of the code can be found in[73,74] and references therein.

1. *Low Mach number correction*

The accuracy of the above schemes and any other schemes can be further enhanced in low-speed subsonic conditions by implementing the low-Mach correction of Thornber *et al.* [75] (henceforth labelled LMC). The low-Mach correction primarily involves an additional computational step that treats the velocity vector via a progressive central differencing of its components. The LMC ensures a balanced distribution of dissipation of kinetic energy in the limit of zero Mach number, thus extending the validity of compressible flow codes to Mach numbers as low as 10^{-5}, and is mainly required for schemes providing accuracy less than 5th-order[73,74].

After the reconstruction of the velocities has been carried out, the reconstructed left and right velocity components at cell-face $(i+1/2)$ are modified according to:

$$\begin{aligned}\mathbf{u}^{L,new}_{i+1/2} &= (\mathbf{u}_s - \mathbf{u}_u)/2\\ \mathbf{u}^{R,new}_{i+1/2} &= (\mathbf{u}_s + \mathbf{u}_u)/2\end{aligned} \tag{5}$$

where

$$\begin{aligned}\mathbf{u}_s &= \mathbf{u}^L_{i+1/2} + \mathbf{u}^R_{i+1/2}\\ \mathbf{u}_u &= \left(\mathbf{u}^L_{i+1/2} - \mathbf{u}^R_{i+1/2}\right) M_{\max}\end{aligned} \tag{6}$$

and the maximum local Mach number, $M_{\max}$, is given by:

$$M_{\max} = \max\left(M^L_{i+1/2}, M^R_{i+1/2}\right)$$

Note that the density and pressure are not altered in any way during this step, thus the internal energy component ($\rho i = p/(\gamma-1)$) remains unchanged. The reconstructed left and right total energies ($e = i + e_k$) are calculated using the modified velocities in the kinetic energy component ($e_k = \mathbf{u}\cdot\mathbf{u}/2$).

2. *WENO implementation*

To address potential numerical instabilities due to the process of choosing an essentially non-oscillatory (ENO) stencil[76], Weighted ENO (WENO) methods were introduced[77,78]. WENO schemes use a convex combination of all the ENO candidate stencils such that the numerical flux is approximated with the higher order of accuracy in smooth regions while still retaining the ENO property in the flow regions near discontinuities; see[79,80] for an overview and further references. For WENO implementations on structured grids, when the solution is locally smooth enough, the convex combination of the stencils of a rth-order ENO scheme results in a $(2r-1)$th-order WENO scheme[77].

Aiming to achieve a balance between accuracy and stability, we enhance the WENO schemes of 3rd and 5th-order of Jiang and Shu [78] ($r = 2, 3$) and 7th, 9th and 11th-order of Balsara and Shu [71] ($r = 4, 5, 6$) by combining the mapped WENO approach of Henrick, Aslam, and Powers [81] (WENO-M) and the relative total variation limiter approach of Taylor, Wu, and Martín [82] (WENO-RLTV). WENO-M recovers the loss of accuracy occurring near smooth critical points. WENO-RLTV reduces the numerical dissipation by using the optimal linear weights in regions sufficiently smooth instead of the nonlinear smoothness-indicator-based weights. The numerical reconstruction can be performed at conservative, characteristic, or primitive variables. The reconstruction of the conservative variables is more common in the literature. However, past research has shown that such practice can lead to inaccuracies in capturing shock waves; see Zanotti and Dumbser [83] and references therein. Similar to other authors[84], we have opted to use the primitive variables in the high-order numerical reconstruction. The characteristics-based variables would be more expensive computationally.

We present below a detailed description of the WENO procedure implemented to obtain the left reconstruction, $q^L_{i+1/2}$, of the primitive variables, $q = [\rho, \mathbf{u}, p]^T$, at cell face $i+1/2$:

1. The *full* (left and right reconstruction) stencil $\left(S^G_{i+1/2}\right)$ is normalized, per variable, according to the transformation function:

   $$S^{Gz}_{i+1/2} = \frac{S^G_{i+1/2} - g_{\min}}{g_{\max}} \tag{7}$$

   where

   $$S^G_{i+1/2} = (q_{i-r+1}, \ldots, q_{i+r})$$

   and

   $$\begin{aligned}g_{\min} &= \min\left(S^G_{i+1/2}\right) - 1\\ g_{\max} &= \max\left(S^G_{i+1/2} - q_{\min}\right)\end{aligned}$$

   and the new kth candidate stencil for the left reconstruction, containing r cell center values, is given by:

   $$S^L_{i+1/2;k} = S^{Gz}_{i+1/2}\left[i-r+1+k, \ldots, i+k\right]$$

   where $k = 0, \ldots, r-1$. Eq. (7) normalizes the values of the candidate stencils before the estimation of the smoothness indicators (IS) in such a way that (i) the maximum value of the full stencil becomes equal to one, i.e. $\max(S^{Gz}_{i+1/2}) = 1$, (ii) the minimum value takes a positive and nonzero value, i.e. $\min(S^{Gz}_{i+1/2}) > 0$, and (iii) the value range scales as originally relative to the maximum. By definition, $g_{\max}$ is always positive and non-zero, and hence Eq. (7) will never result in an undefined operation and cause an exception. Using the above *normalization* of the *full stencil values*, per variable, is found to (i) prevent negative WENO smoothness indicator values, (ii) reduce numerical dissipation, and (iii) simplify the application of the proceeding step. The stencil normalization was found not to affect the MUSCL-type slope limiters.

2. Next, a modified version of the relative total variation (TV) limiting procedure of Taylor, Wu, and Martín [82] is implemented. The TV of each kth candidate stencil is calculated according to:

   $$\mathrm{TV}_k\left(S_{i;k}\right) = \sum_{l=1}^{r-1} \left|q_{i-r+k+l+1} - q_{i-r+k+l}\right| \tag{8}$$

   Eq. (8) is then used to obtain the maximum TV ratio between the candidate stencils:

   $$R(\mathrm{TV}) = \frac{\max\left(\mathrm{TV}_k\right)}{\min\left(\mathrm{TV}_k\right) + \varepsilon} \tag{9}$$

If all of the stencils contain significant discontinuities, then the value of $R(\mathrm{TV})$ can be incorrectly small, i.e. $R(\mathrm{TV}) \approx 1$. Thus, an additional criterion is introduced to avoid such a situation. The linear weights are used provided the following two conditions are satisfied:

$$\text{if } \Big[R(\mathrm{TV}) < A_{\mathrm{RL}}^{\mathrm{TV}} \ \& \ \max\left(\mathrm{TV}_k\right) < B_{\mathrm{RL}}^{\mathrm{TV}} \Big] \text{ then} \quad \omega_k^r = C_k^r \tag{10}$$

According to Ref.[82], $A_{\mathrm{RL}}^{\mathrm{TV}} = 5$, while for the second condition, $B_{\mathrm{RL}}^{\mathrm{TV}} = 0.2(r-1)$, where r is the order of the polynomials used in the $2(r-1)^{\mathrm{th}}$-order WENO. Note that the equation for $B_{\mathrm{RL}}^{\mathrm{TV}}$ is applicable only if the preceding pre-treatment/re-scaling of the candidate stencils is carried out; otherwise, it must be multiplied by $q_{\max}$. In essence, the second condition allows for an average TV of 20% between two neighbouring cells of the local stencils (S_i^G) maximum variable value, but this value can be modified if necessary. Wu and Martin[24] used a value of $B_{\mathrm{RL}}^{\mathrm{TV}} = 0.2$ for their 4th-order bandwidth-optimized WENO implementation in their DNS study.

Eq. (10) assumes that for the linear weights the condition $\sum_{l=0}^{r-1} C_l^r = 1$ is always satisfied.

3. If condition Eq. (10) is not satisfied. The nonlinear weights based on the smoothness indicators of each candidate stencil are computed according to the following two steps:

$$\Omega_k^r = \frac{C_k^r}{(\mathrm{IS}_k^r)^p + \varepsilon}, \qquad \omega_k^r = \frac{\Omega_k^r}{\sum_{l=0}^{r-1} \Omega_l^r} \tag{11}$$

where $p = r$ and $\varepsilon = 10^{-41}$.

The standard WENO weights obtained in Eq. (11) are modified according to the mapped WENO (WENO-M) approach of Henrick, Aslam, and Powers[81] as:

$$\tilde{\omega}_k^r = \frac{\tilde{\Omega}_k^r}{\sum_{l=0}^{r-1} \tilde{\Omega}_l^r} \tag{12}$$

where, using the alternate formulation of Feng, Huang, and Wang[85], the mapped weights are given by:

$$\tilde{\Omega}_k^r = C_k^r + \frac{(\Omega_k^r + C_k^r)^{K+1} A}{(\Omega_k^r - C_k^r)^K A + \Omega_k^r (1 - \Omega_k^r)} \tag{13}$$

and setting $A = 1$ and $K = 2$ results in the original mapping function[81].

4. The reconstructed scaled variable value at the left-side of cell-face $i+1/2$ is given by:

$$q_{i+1/2}^L = \sum_{k=0}^{r-1} \left[\tilde{\omega}_k^r f(q)_k^r \right] \tag{14}$$

where

$$f(q)_k^r = \sum_{l=0}^{r-1} \alpha_{k;l}^r \, q_{i-r+k+l+1} \tag{15}$$

5. Finally, due to the initial *"normalizing"* of the stencil in step 1, the reconstructed values obtained using Eq. (14) needs to be *"re-scaled"* according to:

$$q_{i+1/2}^L = q_{i+1/2}^L \, g_{\max} + g_{\min} \tag{16}$$

WENO reconstruction can lead to spurious oscillations if two or more shocks are too close to each other and WENO cannot choose a single smooth stencil. To remedy this problem, a procedure first introduced by Harten *et al.*[86] is adopted. If the reconstructed density and pressure values differ too drastically from their cell-center average values, the order of the WENO reconstruction is reduced. After completion of the left and right reconstruction procedures at cell-face $i+1/2$, the left and right reconstructed density and pressure values are compared against their respective left and right cell-center values:

$$\left| \rho_{i+1/2}^L - \rho_i \right| > \mathrm{C}_{\mathcal{O}}^{-} \quad \text{or} \quad \left| \rho_{i+1/2}^R - \rho_{i+1} \right| > \mathrm{C}_{\mathcal{O}}^{-} \tag{17}$$

where the order reduction threshold constant is set equal to $\mathrm{C}_{\mathcal{O}}^{-} = 0.7$. If the condition in Eq. (17) is met, then the order of the WENO scheme is reduced according to $(r-1)$. The reconstruction procedure is then repeated for all variables, and the condition is checked again. The process is repeated until Eq. (17) is no longer satisfied. For example, assuming the condition is repeatedly met, a 9th-order WENO would first reduce to 7th-order, then to 5th, 3rd, and finally to the 2nd-order MC MUSCL scheme. Titarev and Toro[87] showed that using the above procedure does not degrade the high order of accuracy for sufficiently smooth solutions.

3. HLLC Riemann solver implementation

The Riemann problem is solved here using the so-called "Harten, Lax, van Leer, and (the missing) Contact" (HLLC) approximate Riemann solver of Toro, Spruce, and Speares[88]. More specifically, the adaptive non-iterative Riemann solver (ANRS) variant proposed by Toro[89] (see §9.5.2) is implemented. The following sequence details the approximate HLLC Riemann solver procedure implemented:

1. To ensure high order near the boundaries for high-order FVM codes, typically, the ghost-cell method is used to apply the boundary conditions (BC). However, even after carefully programming the boundary conditions and reconstruction procedures, computer rounding errors can persist and give rise to differences between the left and right reconstructed states. Therefore, to ensure the appropriate flux, we modify the left and right reconstructed states for the following BCs: symmetry plane (inviscid wall), heated (constant temperature) wall, and adiabatic (zero heat-flux) viscous (no-slip) wall.

   For a symmetry plane, the no penetration condition is implemented for both advective and acoustic waves using the procedure described by Algorithm 1.

```
if Left BC Symmetry then
    $\rho_L = \rho_R$;
    $p_L = p_R$;
    $\mathbf{u}_R = \mathbf{u}_R - (\mathbf{u}_R \cdot \hat{\mathbf{n}})\mathbf{u}_R$;
    $\mathbf{u}_L = \mathbf{u}_R$;
else if Right BC Symmetry then
    $\rho_R = \rho_L$;
    $p_R = p_L$;
    $\mathbf{u}_L = \mathbf{u}_L - (\mathbf{u}_L \cdot \hat{\mathbf{n}})\mathbf{u}_L$;
    $\mathbf{u}_R = \mathbf{u}_L$;
```

Algorithm 1: Ensure symmetry BC flux in HLLC.

In the case of a viscous wall, Algorithm 2 is used instead. For an isothermal wall, the temperature at the ghost cells is linearly interpolated from the interior domain and the wall. In this case, it is advisable to restrict the interpolated temperature range of values to be only positive ($T \in \mathbb{R}_{>0}$), i.e. $T_{\text{ghosts}} > 10^{-15}$, which reduces the likelihood of a non-physical solution from manifesting.

```
if Left BC Viscous Wall then
    $p_L = p_R$;
    if Wall Temperature then $\rho_R = \frac{p_R}{R_s T_W}$;
    $\rho_L = \rho_R$;
    $\mathbf{u}_L = \mathbf{u}_R = 0$;
else if Right BC Viscous Wall then
    $p_R = p_L$;
    if Wall Temperature then $\rho_L = \frac{p_L}{R_s T_W}$;
    $\rho_R = \rho_L$;
    $\mathbf{u}_L = \mathbf{u}_R = 0$;
```

Algorithm 2: Ensure viscous wall BC flux in HLLC; if *Wall Temperature* true isothermal, else adiabatic.

2. An initial estimate of the pressure in the *Star Region*, that is, the region defined in-between the two non-linear convective wave-speeds (or characteristics), can be obtained according to[90]:

$$p_* = \max\left(0, p_{\text{pvrs}}\right) \tag{18}$$

which for curvilinear coordinates p_{pvrs} is obtained according to:

$$\begin{gathered} p_{\text{pvrs}} = \frac{1}{2}\left[p_L + p_R + \left(u_L^{\perp} - u_R^{\perp}\right)\bar{\rho}\bar{s}\right] \\ \bar{\rho} = \left(\rho_L + \rho_R\right)/2\,, \quad \bar{s} = \left(s_L + s_R\right)/2 \end{gathered} \tag{19}$$

where the speed of sound is defined as $s = \sqrt{\gamma p/\rho}$ and $u^{\perp} = \mathbf{u} \cdot \hat{\mathbf{n}}$ is the magnitude of the velocity normal to the cell-face.

The *"averaged"* value of p_* given by Eq. (18), is enhanced by taking into account the local conditions. The ANRS approach[89] introduces two conditions as a means to avoid unnecessary computations, i.e. updating the value of p_* obtained by Eq. (18) with one that is more accurate. The first condition requires that the ratio between the maximum and minimum local reconstructed pressures is greater than a predetermined constant, i.e.,

$$Q = p_{\max}/p_{\min} > Q_{\text{user}}$$

where $p_{\min} = \min(p_L, p_R)$, $p_{\max} = \max(p_L, p_R)$ and it is recommended that $Q_{\text{user}} = 2$. The other condition requires that p_* does not lie between $p_{\min}$ and $p_{\max}$, i.e. $p_* < p_{\min}$ or $p_* > p_{\max}$. However, likewise, to non-differentiable (reconstruction) limiters, they hinder convergence. Instead, the following relation is used immediately after Eq. (18):

$$p_* = \begin{cases} \left[\dfrac{s_L + s_R - \frac{\gamma-1}{2}\left(u_R^{\perp} - u_L^{\perp}\right)}{s_L/p_L^z + s_R/p_R^z}\right]^{\frac{1}{z}} & \overset{\text{(TRRS)}}{\text{if } p_* \leq p_{\min}} \\ \dfrac{g_L p_L + g_R p_R - \left(u_R^{\perp} - u_L^{\perp}\right)}{g_L + g_R} & \overset{\text{(TSRS)}}{\text{if } p_* > p_{\max}} \end{cases}$$

where

$$\begin{gathered} z = \frac{\gamma - 1}{2\gamma}, \quad A_K = \frac{2}{(\gamma - 1)\rho_K}, \quad B = \left(\frac{\gamma - 1}{\gamma + 1}\right) p_K \\ g_K = \left(\frac{A_K}{p + B_K}\right)^{1/2}, \qquad K = L, R \end{gathered}$$

The abbreviations TRRS[89] and TSRS[89,91] stand for the Two-Rarefaction Riemann Solver and Two-Shock Riemann Solver, respectively.

3. Next, we compute the wave-speed estimates according to a modified formulation which combines the approaches of Davis [92] and Toro, Spruce, and Speares [88]:

$$\begin{aligned} S_L &= \min\left(u_L^{\perp} - s_L q_L \,,\, u_R^{\perp} - s_R q_R\right) \\ S_R &= \max\left(u_L^{\perp} + s_L q_L \,,\, u_R^{\perp} + s_R q_R\right) \end{aligned} \tag{20}$$

where

$$q_K = \begin{cases} 1 & \text{if } p_* \leq p_K \\ \left[1 + \dfrac{\gamma+1}{2\gamma}\left(\dfrac{p_*}{p_K} - 1\right)\right]^{1/2} & \text{if } p_* > p_K \end{cases} \tag{21}$$

Eq. (20) slightly increases the numerical diffusion as it permits a greater range but has favourable stability in very high-speed flows and particularly near strong shock-waves.

Using the above, the intermediate *"missing"* wave-speed, S_*, and associated HLLC fluxes are computed according to Toro [89].

III. HIGH-RESOLUTION SIMULATIONS AT MACH 6

The problem case concerned hypersonic flow over a flat plate at Mach 6 subjected to von Kármán atmospheric spectrum at the inlet. We compare ILES and DNS results in the

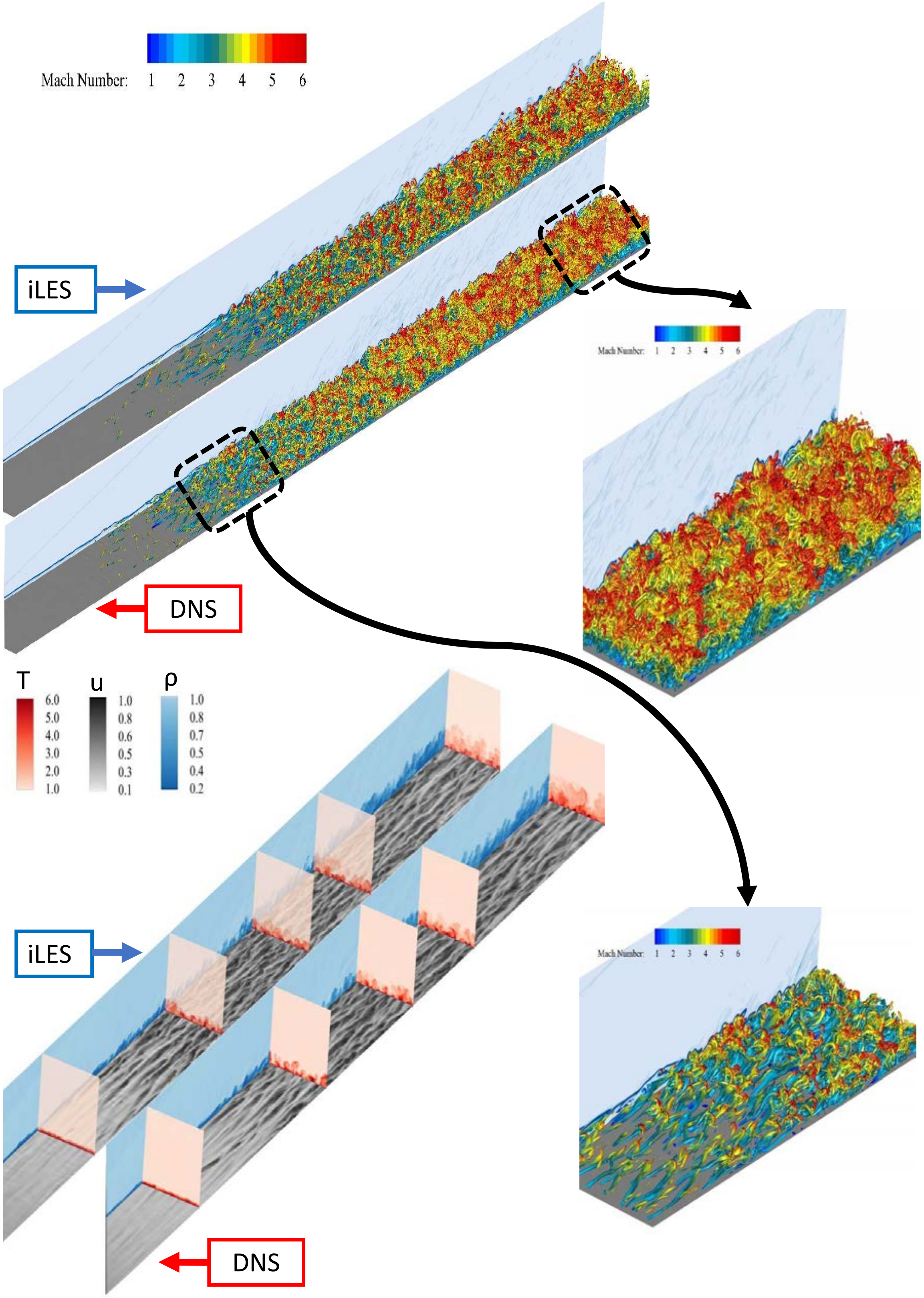

FIG. 1. Comparison of instantaneous plots between ILES and DNS. Upper figures and zoom-ins are isosurfaces of compressible Q-criterion coloured by Mach number. The density gradient is also plotted in blue scale on the graph's side, highlighting the transition region. The lower left figures are the contour plots of density and streamwise velocity near the wall and temperature contour plots at various cross-sections of the simulation domain.

TABLE I. Simulation parameters for hypersonic flow over a flat plate at altitude 11651m.

x_l (mm)	u_∞ (m/s)	P_∞ (kPa)	T_∞ (K)	M_∞ (-)	ρ_∞ (kg/m^3)	T_w (K)	Re_{x_l} (-)	Tu (-)
2.0	1,769.92	19.417	216.64	6.0	0.3124	1600	77,791	1%

same CFD code (CNS3D) using the same simulation parameters, with the only difference being the mesh resolution. This comparison allows the examination of the accuracy of high-fidelity approaches for predicting the complexity of transition, turbulence, and associated acoustic effects. The turbulence intensity of the freestream velocity at the inlet is $Tu = 1\%$. Regarding acoustic loading, it has been shown that the inlet's turbulent intensity affects the maximum acoustic load location but not the actual value[63]. A comprehensive study (incompressible flow) on free stream turbulence and TBL can be found in[93]. Based on the freestream properties (Table I) and the reference length $x_l = 2$ mm, the incoming flow has a Reynolds number of $Re_{x_l} = 77{,}791$. The reference length is calculated from the leading edge of the plate. We implement periodic boundary conditions in the spanwise direction (z). In the wall-normal direction (y), we use a no-slip isothermal wall (with a temperature T$_w$ of 1600 K, near the adiabatic value)[94]. High-order implementation of the boundary conditions requires fictitious cells inside the wall. The velocity components on these cells are linearly extrapolated from the computational cells inside the domain. The temperature is also linearly extrapolated using the specified wall temperature. The density is calculated from the equation of state considering a zero pressure gradient normal to the wall. We apply supersonic outflow conditions at the outlet and far-field boundaries. The same methodology was also recently used with the digital filter approach to study the flow and acoustics of supersonic shock/boundary-layer interactions[5].

A qualitative comparison of the flow development for both ILES and DNS is shown in Figure 1 using the isosurfaces of compressible Q-criterion and contour plots velocity, density and temperature. Transition to turbulence is slightly delayed in the ILES case than the reference DNS case, while a coarser grain of turbulent structures is captured in the turbulent region (Figure 1). However, considering the 50 times coarser mesh utilized by ILES, the accuracy and details captured are impressive. If we focus on the temperature, density and velocity contour plots, the results are indistinguishable between the two cases.

Figure 2 shows that DNS predicts an earlier pressure fluctuation peak with an increased magnitude compared to ILES. However, ILES and DNS converge to the same pressure fluctuations in the fully turbulent region. This supports our findings on correcting the theoretical model in[63] and does not alter our previous conclusions. The above result demonstrates that ILES can predict pressure fluctuations and acoustic loading in fully turbulent areas without compromising accuracy compared to the intensive DNS.

In Figure 2, we have included the (approximate) ILES error associated with different numerical methods ranging from 5th to 9th-order accuracy. Note that the estimated error has emerged from the authors' extensive experience using high-order methods for iLES in various compressible flows[9,62,73,95,96]. The error ranges from ±2% to ±5% depending on the flow region, transitional or turbulent.

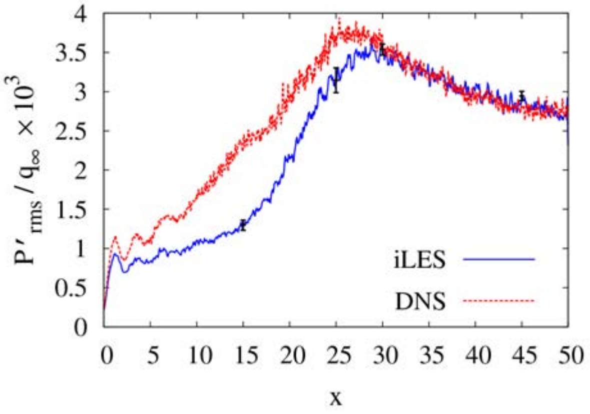

FIG. 2. Comparison of pressure fluctuations along the plate between ILES and DNS. The error bars (black color) on the iLES results correspond to ±5% and ±2% of the local value for the two selected points in the transition and turbulent region.

Pressure fluctuations have an essential effect on the structural response of hypersonic structures. Compared to DNS, the ILES delay in transition does not affect (P'_{rms}) in the turbulent region. Since the results show that iLES is sufficiently accurate to predict pressure fluctuations in the turbulent regime, the delay in transition is not expected to affect the structural response. To corroborate the above, future aerostructure simulations that involve ILES over flexible panels are required.

We analyze each pressure history signal as a single-point spectrum in the frequency domain, which is defined by

$$\Phi(\omega) = \frac{1}{2\pi} \int_{-\infty}^{\infty} \overline{P'(x,y,z,t)P'(x,y,z,t+\tau)} e^{-i\omega\tau} d\tau, \qquad (22)$$

where τ is a time delay and ω is the radial frequency. Initially, we evaluate the ILES approach's accuracy in direct comparison with DNS results at the same locations (see Figure 3). Despite the significantly lower resolution in space and time, the iLES results agree with the DNS in the low- and medium-frequency regimes. The ILES underestimates the spectrum's amplitude in higher frequencies, while we cannot resolve very high frequencies due to the mesh size. The spectrum roll-off follows the same scalings in all cases, as shown in more detail below. It is worth mentioning that DNS can capture at over 21 MHz.At the same time, ILES can resolve frequencies up to 4.3 MHz, which is still significantly higher than most experimental sensors and measurement techniques can achieve[39,98,99]. The mesh resolution and time limit the frequency range accurately captured by the simulations. The maximum resolved frequency depends on mesh resolution, hence the five-fold difference between ILES and DNS. The minimum resolved frequency depends on time; longer simulation times resolve lower frequencies. In the present results, the minimum frequency captured is around 350 kHz.

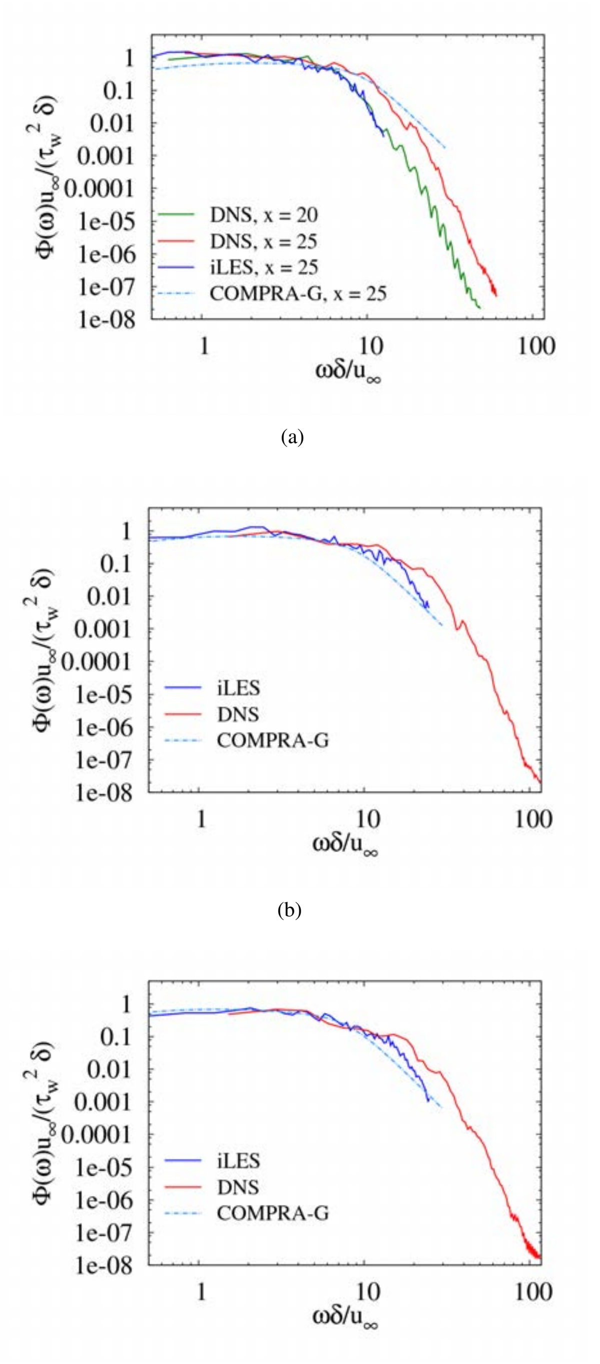

(a)

(b)

(c)

FIG. 3. Comparison of spectra between ILES, DNS and the COMPRA-G model at various locations in the transitional and fully turbulent regime. In a) we also present the spectrum of the pressure history at location $x = 20$ from DNS data: a) $x = 25$ and $\delta = 1.05$ mm based on Bies[97] empirical correlation for the calculation of δ; b) $x = 30$, $\delta = 1.21$ mm; c) $x = 45$, $\delta = 1.66$ mm.

Figure 3(a) shows the spectra at the peak of the transition for the DNS case ($x = 25$). Knowing from the analysis in the previous sections that iLES reaches the peak at a later point, we include in the same plot the DNS results from location $x = 20$ where the magnitude of the pressure fluctuations is closer to that of iLES at $x = 25$. In that case, the spectra are identical to the maximum resolution that iLES can achieve. This is a possible indication that the mismatch at higher frequencies when we compare the spectra between iLES and DNS at the same locations could be potentially attributed to the iLES delay in reaching the transition's peak.

In the same figures, we include a semi-empirical wall-pressure spectra model (COMPRA-G), which the authors have extended based on Goody's model[100]. More discussion about semi-empirical models and COMPRA-G can be found in[101]. The proposed model produces a scaling behaviour based on the established pressure spectrum scaling for zero pressure-gradient, fully turbulent subsonic and supersonic flows. The proposed COMPRA-G also applies to high-speed flows, as we include compressibility effects. COMPRA-G also retains excellent prediction capabilities at lower-speed flows down to the incompressible limit ($M = 0.1$)[101].

COMPRA-G consists of one equation, based on Howe's[102] and Goody's[100] past studies:

$$\frac{\Phi(\omega)u_\infty}{\tau_w^2\delta} = \frac{C_2\chi^2}{[\chi^{0.75}+C_1]^{3.7}+[C_3R_T^{C_{RG}}\chi]^7}, \tag{23}$$

where $C_1 = 0.5$, $C_2 = 3.0$ and $C_3 = 1.1$ are empirical constants, $\chi = \omega\delta/u_\infty$, $R_T = \delta u_\tau^2/(\nu_w u_\infty)$ and $C_{RG} = -0.49$ for supersonic and hypersonic flows. In the case of incompressible flows, $C_{RG} = -0.57$. The authors have shown[101] that all the necessary parameters for the calculation of COMPRA-G can be based on freestream properties, the distance from the leading edge and empirical correlations like the one proposed by Bies[97] for the boundary layer thickness

$$\delta = 0.37xRe_x^{-0.2}\left[1+\left(\frac{Re_x}{6.9\times 10^7}\right)^2\right]^{0.1}. \tag{24}$$

We show characteristic values of δ for each location in Figure 3 based on Eq. 24, where x is the distance from the plate's leading edge in meters. The spectra from the iLES and DNS calculations have been non-dimensionalized based on parameters calculated during the simulations at the corresponding locations.

The COMPRA-G empirical model can capture the low and medium frequency regimes with high accuracy based only on freestream properties usually known or much easier to obtain. High frequencies are not captured correctly as the model has been designed with an ω^{-5} scaling, while hypersonic flows seem to have steeper high-frequency scalings. COMPRA-G can predict the pressure spectra below fully turbulent boundary layers and in challenging transitional regimes. Such a model could be used for quick approximations when focusing on low and medium-frequency regimes without more expensive simulations or experiments.

The spectra results can also be analyzed in comparison with the theoretical predictions for fully turbulent flows[103], and various observations[104]. Bull[104] isolated four different regions of low, mid (which includes the spectral peak), mid-to-high overlap, and high frequencies, with corresponding spectrum slopes of ω^2, ω^0, ω^{-r} ($r = [0.7, 1.1]$), and ω^{-t} ($t = [7/3, 5]$), respectively. The turbulent motion influences the low-frequency region in the outer part of the boundary layer. The viscosity and turbulent motion affect high frequencies in the inner part of the boundary layer.

According to the theoretical arguments made by Ffowcs-Williams[105] for compressible flows, the scaling should be $\omega \to 0$ in the low-frequency region. This observation has been confirmed by experimental and numerical studies of supersonic and hypersonic turbulent boundary layers[63,106–109]. The above contrasts the Kraichnan-Phillips theorem for incompressible flows[104,110,111], which suggests ω^2.

The mid-to-high overlap frequency region appears at sufficiently high Re_θ values, and the spectrum varies as ω^{-r} with $r = 0.7$ to 1.1, influenced by the local Reynolds number. This region is associated with pressure-induced eddies in the logarithmic region of the boundary layer. Its scaling behaviour was predicted by Bradshaw[112] and was verified theoretically[113] and experimentally[108,114].

Following the ω^{-r} region, the spectrum becomes $\omega^{-7/3}$, henceforth called "acoustic-transition", which was also predicted for isotropic turbulence by Batchelor[115] and has also been observed in various experiments[116–118], as well as verified by numerical calculations of supersonic turbulent boundary layers[106,109]. The spectrum decays rapidly at high frequencies, reaching a slope proportional to ω^{-5}. Sources in the sublayer ($y^+ < 20$) contribute to this frequency region according to the theoretical prediction of Blake[103], with the scaling being validated experimentally, as well[114,119].

The full details were presented in[10,120,121], and a summary of the key findings is provided below.

1. The results shed light on the accuracy of high-resolution simulation approaches such as Implicit Large Eddy Simulation and Direct Numerical Simulation for hypersonic transitional and turbulent flows and associated acoustic loading near-wall effects.

2. ILES can produce highly accurate flow and acoustic metrics results even though a 50 times reduced mesh resolution compared to DNS.

3. ILES slightly under-predicts the transition peak and delays the transition.

4. ILES predicts the correct spectrum roll-off for transitional and turbulent hypersonic boundary layers. However, it underpredicts high-frequency amplitude due to mesh resolution constraints at high frequencies.

5. The acoustic spectra scaling at Mach 6 differs from incompressible flow across frequencies. Therefore, incompressible models should not be used in high-speed flows.

6. The proposed wall-pressure spectra model COMPRA-G that includes compressibility effects gives good estimates of the low and medium frequency regimes based only on freestream properties. This makes its implementation extremely straightforward and fast, avoiding the need for costly computer simulations.

7. Since the iLES captures the near-wall acoustic spectrum roll-off at low/medium frequencies, it would be appropriate for modeling structural dynamic loading.

Furthermore, we performed wavelet analysis of the high-resolution data and the results were published in[66] and discussed in[121]. We used the coherent vortex extraction (CVE) method to remove noise from signals in wavelet space. The main idea is to decompose the flow into coherent (represented by a few wavelet coefficients) and incoherent parts (noise) using wavelet filtering of the vorticity field. The evolution of the coherent part of the flow is computed deterministically, whereas the influence of the incoherent background flow is modeled statistically. No model is needed for coherent structure definition. Instead, the noise should be modelled more trivially and is assumed to be additive, Gaussian and white. Wavelets are basis functions localized in both physical and wave-number spaces.

DNS data of turbulent compressible boundary layer flow were analyzed using the CVE method. The flow was decomposed into coherent and incoherent parts by thresholding the wavelet coefficients with one scale in three spatial directions. We found that few wavelet coefficients are sufficient to represent the flow's coherent structures. Furthermore, the coherent component carries most of the energy. The PDFs of the vorticity components are skewed for the coherent part (and total). Instead, the PDFs of the incoherent components are symmetric for all vorticity components in both the transition and turbulent region.

The incoherent part of vorticity appears without an apparent topological structure and low amplitude. However, further analysis shows a correlation between the pressure fluctuations and the incoherent vorticity — the transition region had the highest correlation at $y^+ \approx 4$. Details can be found in[66].

IV. COMPRESSION RAMP

The flow data concerned the supersonic flow over a flat plate followed by a "compression" ramp at a Mach number of $M_\infty = 2.9$ and a Reynolds number of $Re_{\delta_0} = 38,737$ based on the freestream conditions and incoming turbulent boundary layer thickness. The DNS data set used in the analysis was presented in a previous study[5].

An illustration of the resolved turbulent flowfield is given in Fig. 4. The streamwise distribution of the time and spatially averaged mean wall pressure (Fig. 6) shows that the W9 scheme provides more accurate results than the MUSCL schemes. The W9 results are in excellent agreement with the DNS of Wu and Martin [24] and the experiment of Bookey *et al.* [17]. M5LM (green line) does not correctly capture the location of the separation bubble because the resolution of finer flow structures is weaker compared to W9. The above numerical behaviour leads to the formation of more energetic large-scale turbulent structures, which are responsible for *"blowing"* the shock in the downstream direction. Our experience is that W9 can attain the same accuracy with the M5LM while using a coarser mesh.[9,64,101,122,123]

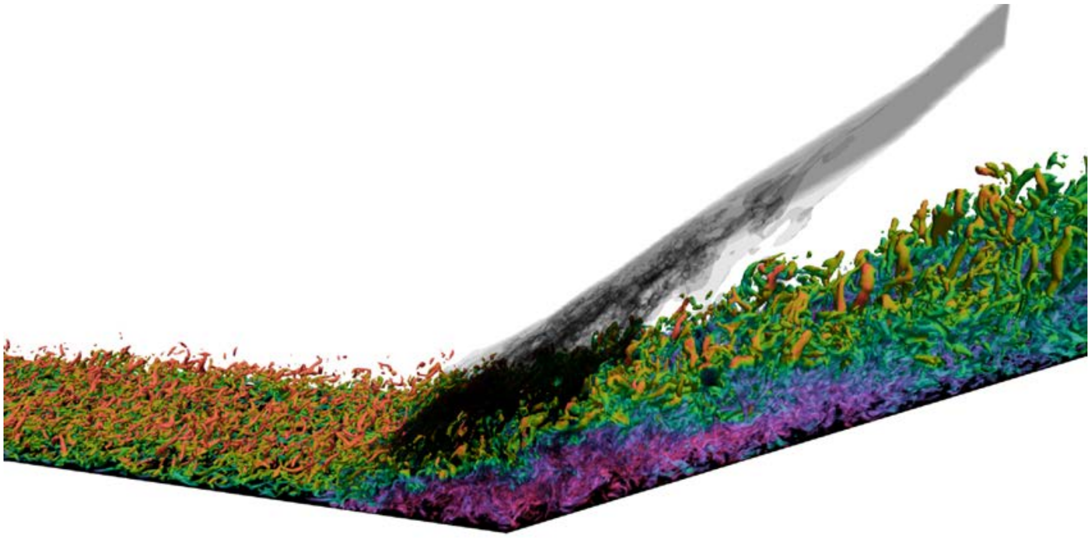

FIG. 4. Semi-transparent black iso-surfaces depicting the incident shock wave front and Mach number coloured iso-surfaces of Q-criterion illustrating the resolved turbulent scales at the supersonic boundary layer interaction (SBLI) region.

The friction coefficient, C_f, is plotted in Fig. 7. The low-Mach number correction (LMC) does not improve C_f significantly due to the subsonic region of the undisturbed TBL confined within the viscous sublayer. Though the subsonic region at the separation bubble can extend as high as $0.6\delta_0$, also evident by the sonic line depicted in Fig. 5, the position of the shock remains largely unaffected. Any loss of accuracy in this critical region should lead to significant errors in the SBLI dynamics and downstream turbulent flow characteristics. Therefore, the LMC offers only a marginal improvement in accuracy in this case.

The spatial order of the scheme has a substantial effect on simulation accuracy. At $x = -8\delta_0$, the W9 accurately predicts the skin friction coefficient, $C_f \approx 0.0022$, whereas both the M5 and M2LM underestimate it: $C_f \approx 0.00195$ and 0.0019, respectively. The LMC improves the skin friction coefficient of the fifth-order MUSCL scheme (M5LM) by 2.5% ($C_f \approx 0.002$). The corresponding value quoted by the DNS[24] and experimental[17] studies was $C_f \approx 0.00217$ and 0.00225, respectively. The W9 gives the closest agreement to the experimental locations at which the C_f changes sign, which indicates the extent of the SBLI separation bubble. The results suggest that the ability of the scheme to accurately resolve the turbulent structures in the supersonic region of the "undisturbed" TBL largely determines the accuracy in the prediction of the size and location of the separation bubble.

Nonetheless, the computational overhead of the LMC is found to be small, as also observed in previous studies[73,74]. The increasing accuracy of the W9 compensates for the higher computational cost. As shown in[73,122], low-order schemes require much finer grids and smaller time-step sizes, ultimately turning into an increased computational cost.

A qualitative comparison of the schemes' accuracy can be accomplished by plotting the isosurfaces of the coherent turbulent structures (vortices). We have used the compressible Q_M–criterion[124,125], defined as:

$$Q_M = Q + II_S > 0 \tag{25}$$

where the standard (incompressible) Q–criterion is given by:

$$Q = \frac{1}{2}\left(\|\Omega\|^2 - \|\mathsf{S}\|^2\right) \tag{26}$$

and II_S is the second invariant of the strain-rate tensor S

$$II_S = \frac{1}{2}\left[\mathrm{Tr}\left(\mathsf{S}\right)^2 - \mathrm{Tr}\left(\mathsf{S}^2\right)\right] \tag{27}$$

$\nabla\mathbf{u}$ consists of the symmetric strain-rate tensor S and anti-symmetric vorticity tensor Ω:

$$\mathsf{S} = \frac{1}{2}\left[\nabla\mathbf{u} + (\nabla\mathbf{u})^T\right], \quad \Omega = \frac{1}{2}\left[\nabla\mathbf{u} - (\nabla\mathbf{u})^T\right] \tag{28}$$

and the standard Frobenius tensor norm for a tensor T in three dimensions takes the form

$$\|\mathsf{T}\| = \sqrt{\mathrm{Tr}\left(\mathsf{T}\mathsf{T}^T\right)} \tag{29}$$

The Q_M isosurfaces (Fig. 8) reveal that increasing the spatial order of the scheme provides a greater abundance of flow structures, particularly upstream of and around the SBLI. The differences become less apparent in the relaxation region downstream of the SBLI. The W9 resolves much finer scale vortices throughout the height of the TBL. As a result, the W9 transfers and *"injects"* more effectively into the viscous sublayer a larger amount of mean kinetic energy, leading to an increase in the resolved wall shear-stress (Fig. 7). The mechanism is that W9 captures the details of the vortices at the turbulent/nonturbulent interfaces (TNTI), which carry turbulent fluctuations into the TBL. This process occurs simultaneously with the fluctuations in the freestream, which are radiated from inside the TBLs as reported by Duan, Choudhari, and Zhang [106].

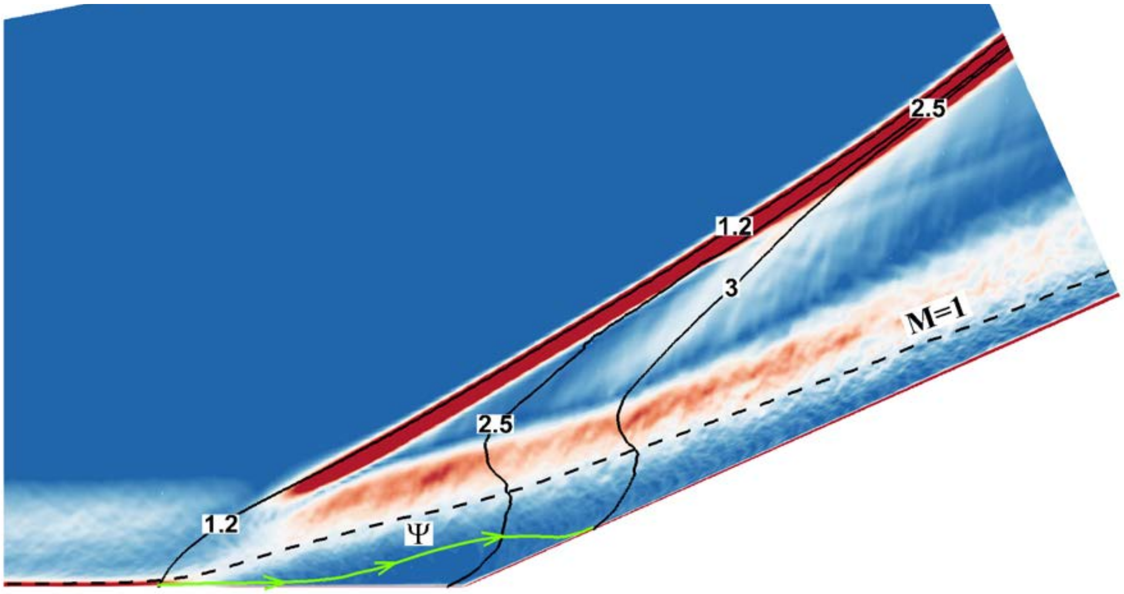

FIG. 5. Contour plot of mean density gradient magnitude ($\nabla\bar{\rho}\ \delta_0/\rho_\infty$); solid lines of $\bar{p}/p_\infty$, dashed sonic line ($M = 1$), green line with arrows depicts streamline Ψ over the recirculation bubble

.

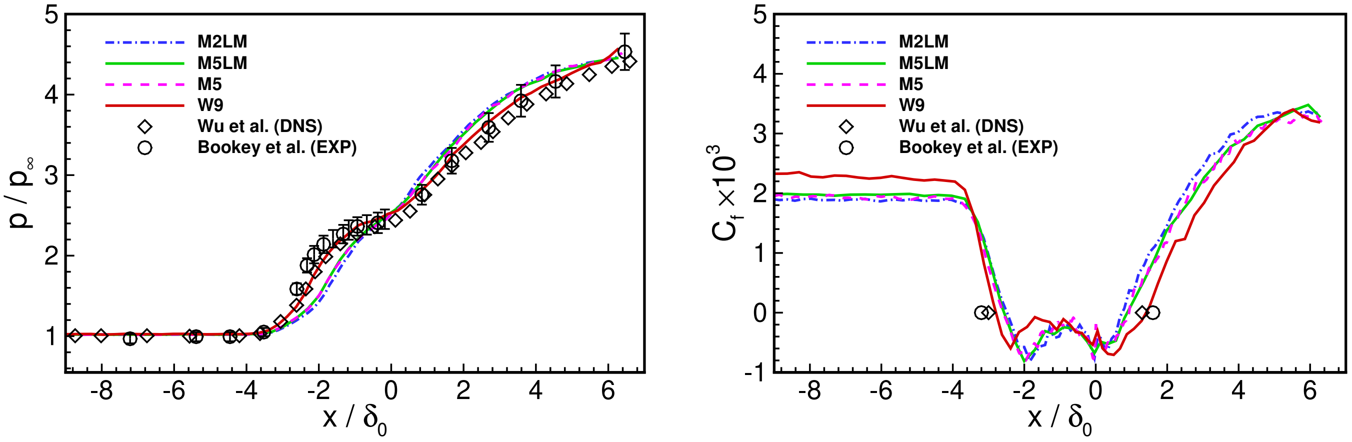

FIG. 6. Normalized mean wall pressure, p/p_∞, distribution along the streamwise direction.

FIG. 7. Skin friction coefficient, C_f, distribution along the streamwise direction.

We have performed power spectral density (PSD) analysis of the surface pressure loading only for the W9 scheme, as it provides the best agreement with the experimental measurements[17]. The position of the numerical pressure probes is shown in Fig. 9: one before SBLI at $x/\delta_0 = -6.9$ (Point 1), and two before and after the separation bubble onset at $x/\delta_0 = -2.98$ (Point 2) and -2.18 (Point 3), respectively. The separation bubble onset is when the friction coefficient, C_f, changes sign. For the W9 scheme, it occurs approximately at $x/\delta_0 \approx -2.785$.

The PSD at the three locations is plotted in Fig. 10. Both pressure and frequency have been non-dimensionalized using outer-layer scaling; the freestream pressure normalizes the fluctuating pressure signal, $p'(t)/p_\infty$, while the frequency, f, is normalized according to $St = f\,\delta_0/u_\infty$, where St is the dimensionless Strouhal number. We show the frequency up to $St\sim 10$, which is near the grid resolution cut-off at the wall, i.e. $f_{\max} \sim s_w/(2\Delta y_w)$, where $s_w = \sqrt{\gamma R_s T_w}$ is the speed of sound at the wall and Δy_w is the largest cell edge; in this case in the spanwise (y) direction.

For the undisturbed supersonic TBL, the peak PSD is at the non-dimensional frequency of one. The energy is slowly transferred from the large scales to $f \approx 1$ (henceforth $f \equiv St$). In general, the PSD follows the established cascade[104] that has been investigated for compressible flows[123], and defines four distinct frequency domains:

1. Low frequency f^x: it is influenced by the turbulent motion in the outer part of the boundary layer, while the

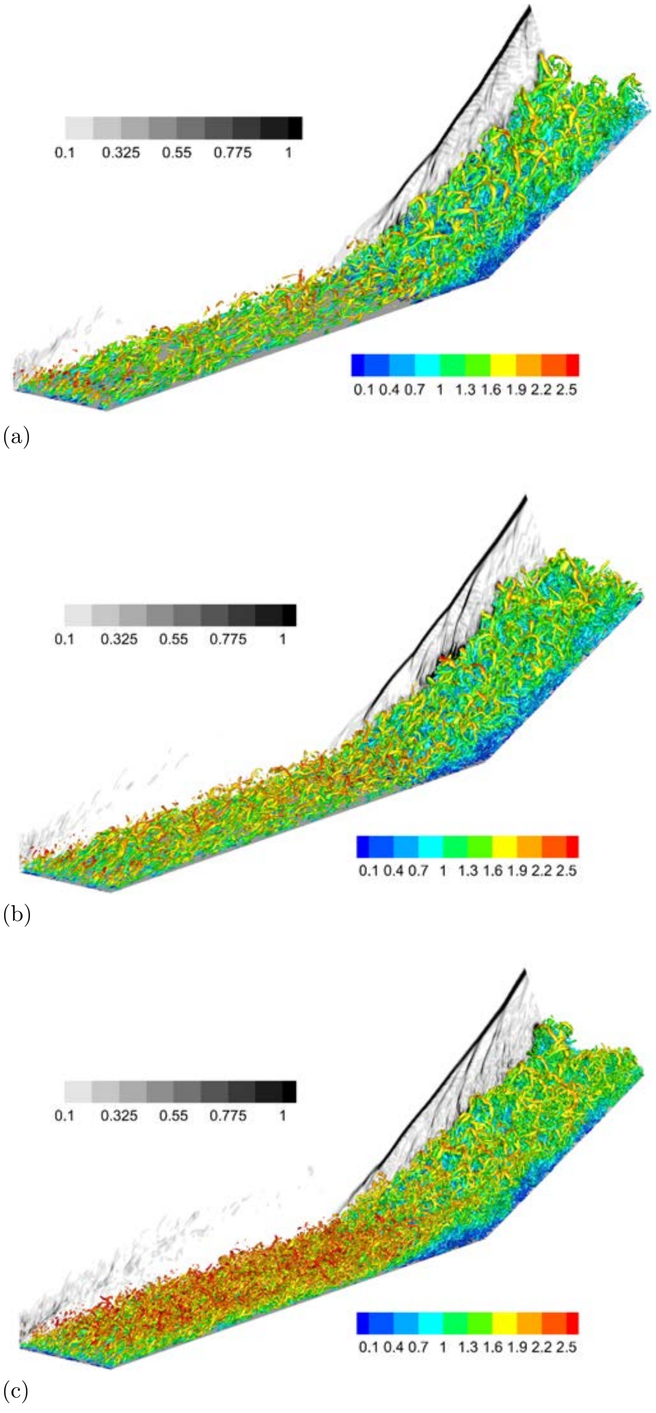

FIG. 8. Isosurfaces of Q_M-criterion $\left(2U_\infty^2/\delta_0^2\right)$ coloured by Mach number and 2D (x-z) contour plane of density gradient magnitude $|\nabla\rho|\ \delta_0/\rho_\infty$ in grayscale using schemes (a) M2LM, (b) M5LM, and (c) W9.

viscosity and turbulent motion influence high frequencies in the inner part. For incompressible flows $x = 2$, while for compressible flows $x \to 0$.

2. Mid frequency: it includes the spectral peak (f^0);
3. Mid-to-High overlap frequency f^{-r} where $r = [0.7 - 1.1]$: it appears at sufficiently high Re values and r is influenced by the local Reynolds number. This region is associated with pressure-induced eddies in the logarithmic region of the boundary layer.

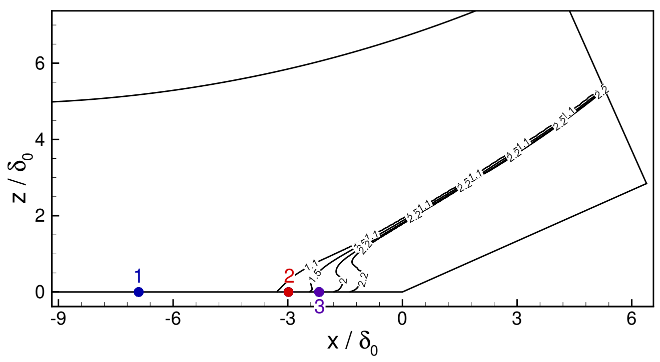

FIG. 9. Illustration of the location of the numerical probes relative to the SBLI; contour lines of p/p_∞.

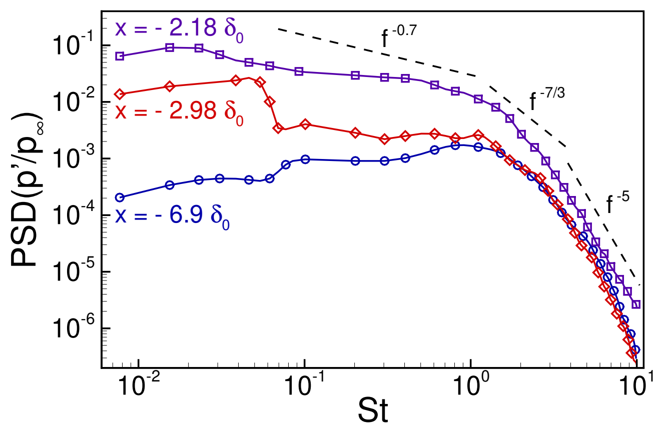

FIG. 10. Power spectral density (PSD) of pressure signal at the three probe locations; Welch function.

4. High frequency f^{-s}: The spectrum scales with $s = 7/3$ in a region called "acoustic-transition". At higher frequencies, the spectrum decays more rapidly ($s = 5$) due to the viscous sublayer ($z^+ < 20$) and weaker compressibility (local mean Mach number < 1).

Figure 10 reveals that the high-frequency domain scales as f^{-5} in all three locations. The same behavior was also observed by Bernardini, Pirozzoli, and Grasso [109]. Inhibition of the higher frequencies is not observed downstream of the separation zone due to the sustained high-speed flow after the oblique shock. This effect is in contrast to the case of a normal shock, also associated with subsonic flow pocket as previously reported[109].

The mid-to-high frequency band (undisturbed TBL) is found to be very narrow since the Reynolds number is not sufficiently high for it to become perceptible. A much broader mid-to-high overlap region forms at the third point within the separation region, attributed to the break-down and redistribution of the large-scale (or low-frequency mode) energy content previously formed at the front of the separation zone (point 2). Although the mean streamwise velocity at position 2 is positive, its instantaneous variation contains negative values. The above suggests that the separation bubble's leading edge oscillates in the streamwise direction over time.

The abrupt increase in the PSD content at the low-end frequency range of the wall pressure signal at $x = -2.98\delta_0$ (Fig. 10 - red line), alludes to the presence of a large scale structure. This is in agreement with the observations made by Bernardini, Pirozzoli, and Grasso[109] and further supported by the similarity of the near-wall pressure fluctuation PSD in the mid-to-high-end frequency band between the λ-shock foot ($x = -2.98\delta_0$) and the undisturbed supersonic TBL ($x = -6.9\delta_0$).

The speed of sound at the wall (point 2) and the low-end frequency range $f \in [0.04, 0.08]\, u_\infty/\delta_0$ over which the PSD abruptly decreases, suggest a flow structure of a time-scale of $[12.5, 25]\, \delta_0/u_\infty$. We have ruled out the unsteadiness of the recirculation vortex within the separation zone as the source of the sudden frequency change at point 2. This is because the time required for a full convective recirculation (of the outer streamline) corresponds to the significantly lower frequency of $\sim 0.01 u_\infty/\delta_0$.

Given the above, we believe an acoustic (pressure wave) mechanism exists. The acoustic propagation time required to travel along streamline Ψ from the separation point to the reattachment position in the relaxation region can be estimated by carrying out a line integral along the streamline (path) Ψ joining $(x,z)/\delta_0$ from $\sim(-2.98, 0.028)$ to $\sim(1.368, 0.623)$:

$$\Delta t_\Psi = \int_\Psi (\gamma p/\rho)^{-1/2}\, \mathrm{d}\psi \tag{30}$$

where $\mathrm{d}\psi$ is the length of a discrete segment along streamline Ψ, i.e. $\mathrm{d}\psi = \sqrt{\mathrm{d}x^2 + \mathrm{d}z^2}$.

Equation (30) gives a time-scale of $\Delta t_\Psi \approx 8\, \delta_0/u_\infty$. Note that the relatively large region of subsonic Mach number post-SBLI allows acoustic waves to propagate upstream of the reattachment towards the SBLI. The mean convective transport is ignored since its effect on the acoustic wave propagation cancels out when carrying out both forward and backward integration along the streamlined path.

Assuming that the acoustic wave travels along streamline Ψ from the point of the mean flow separation to mean reattachment and back, it gives us an estimated time-scale of $\sim 16\, \delta_0/u_\infty$. The above is within the observed low-frequency range $[12.5, 25]\, u_\infty/\delta_0$ found to correspond to the abrupt increase in the pressure fluctuation PSD at the λ-shock foot in Fig. 10. We can obtain a value closer to the upper range value of $25\, u_\infty/\delta_0$ by integrating the acoustic speed propagation upstream along the wall surface. Nonetheless, Δt_Ψ does not constitute sufficient evidence that unequivocally proves that the observed low-frequency mechanism at the λ-shock foot is induced by pressure reciprocity between the SBLI separation and re-attachment regions. The exact physical mechanism leading to this phenomenon is not yet well understood, and further analysis is required.

Furthermore, we used this data to perform wavelet analysis similar to the flat panel. The results of this study were presented in the publication[67] and Year 3 report[126].

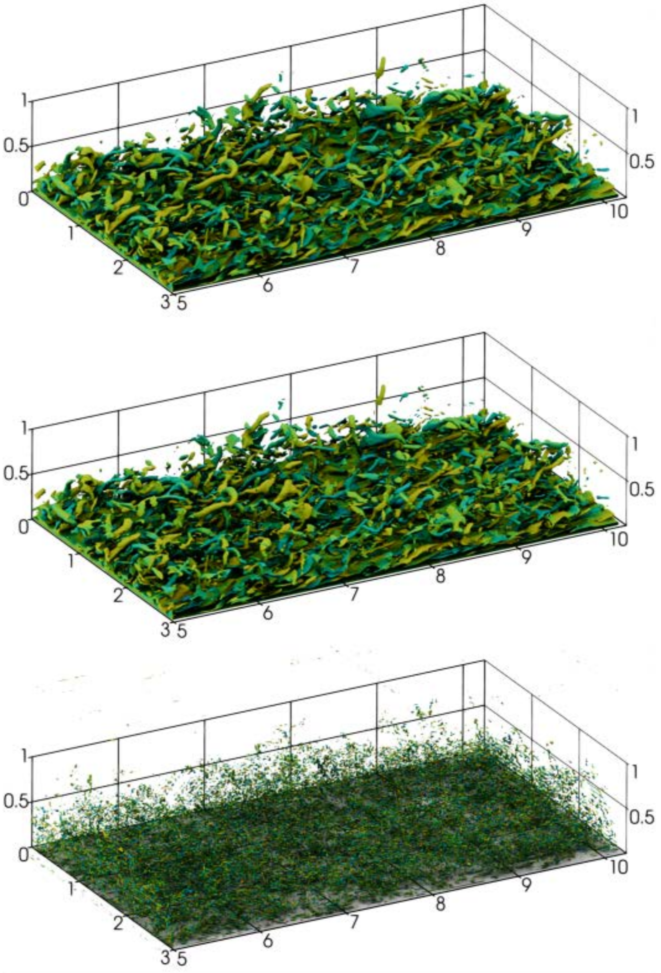

FIG. 11. Total, coherent, and incoherent fields of the absolute vorticity value for the turbulent region $x/\delta_0 \in [5-10]$. Isovalues for total and coherent parts are: $|\omega| = 5.0$, for incoherent part $|\omega|_{\text{inc}} = 0.9$.

The coherent vorticity extraction (CVE) performed denoising of the vorticity field, $\boldsymbol{\omega}(\boldsymbol{x}) = \nabla \times \boldsymbol{V}$ in the wavelet space. We apply the wavelet method to near-wall analysis based on Morkovin's hypothesis[66,127–129], according to which a value of density fluctuations less than 0.1 implies that the turbulence structure near the wall is nearly that of incompressible flows. The near-wall root-mean-square fluctuations are less than 0.06-0.07 (dimensionless).

In Figs. 11, 12 and 13 the visualisation of the results of CVE in the different regions are presented. The total, coherent and incoherent parts of the absolute value of vorticity are shown on the plots from top to bottom. As one can see, the incoherent part of the vorticity is much weaker than the total and coherent parts of the vorticity fields. The isosurface values for the incoherent parts are reduced by six compared to the coherent and total parts of vorticity. The PDFs' total and coherent parts were discussed in detail in[67] and in the Year 3 report[126]. The key findings are summarised below.

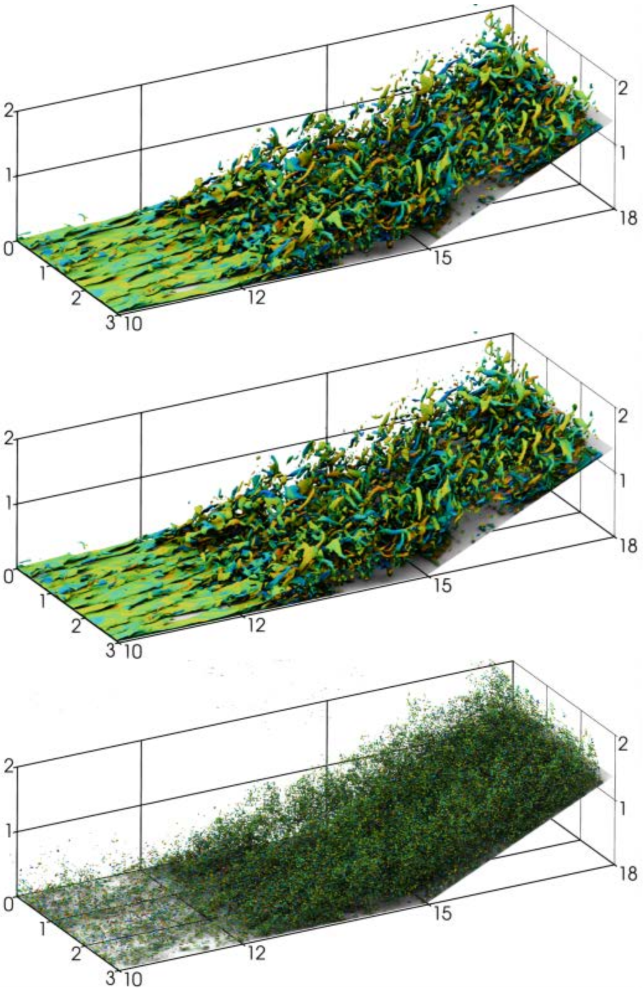

FIG. 12. Total, coherent, and incoherent fields of the absolute vorticity value for the turbulent region $x/\delta_0 \in [10-18]$. Isovalues for total and coherent parts are: $|\omega| = 10.0$, for incoherent part $|\omega|_{\text{inc}} = 1.5$.

- DNS data of supersonic flow can be useful in giving insight into the role of vorticity in SBLI.
- The flow can decomposed into coherent and incoherent parts by thresholding the wavelet coefficients.
- The few wavelet coefficients are sufficient to represent the flow's coherent structures that carry most of the flow energy.
- The PDFs of the vorticity components are skewed for the coherent parts and total fields, and they are perfectly superimposed, showing that the coherent vorticity field preserves the flow statistics.
- The PDFs of the incoherent components are symmetric for all vorticity components for the whole flow.
- The incoherent part of vorticity appears without an apparent topological structure and low amplitude. However, the analysis shows a correlation between the wall-pressure fluctuations and the incoherent part of vorticity

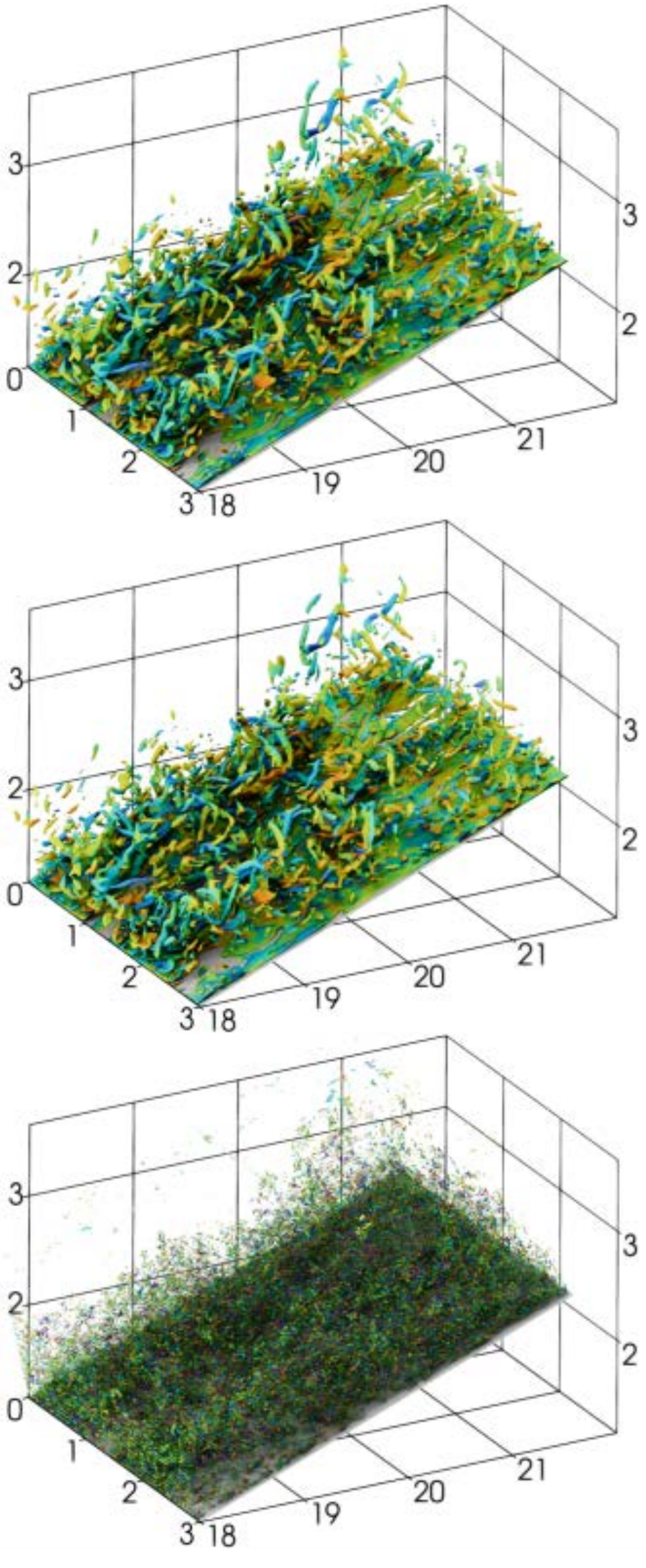

FIG. 13. Total, coherent, and incoherent fields of absolute vorticity values for the turbulent region $x/\delta_0 \in [18-21]$. Isovalues for total and coherent parts are: $|\omega|_{\text{coh}} = 10.0$, for incoherent part $|\omega|_{\text{inc}} = 1.5$.

at different positions from the wall. The highest correlation occurred when $y^+ \simeq 4.3$ ($y = 0.005\delta_0$) for the streamwise and wall-normal vorticity components.

- Our idea regarding a potential correlation of the pressure fluctuations P and the incoherent vorticity $|\omega|_{\mathrm{inc}}$ is speculative. However, the results show a correlation, which indicates that the incoherent vorticity component carries physical information related to pressure fluctuations, thus to near-wall acoustics.

- Furthermore, we believe that the thermodynamic properties of the wall would affect this relationship. If a further investigation proves the above true, we could recover from the velocity field, the incoherent vorticity, and the sound properties of the field.

V. RC-19 CASES

The primary objective of the RC-19 simulations is to reproduce and study the aeroelastic response of a thin panel exposed to turbulent flow with cavity pressure modulation. Low-frequency shock oscillations are a documented aspect of SBLI and a potential concern for FSIs. The RC-19 experimental results were used to develop models to predict conditions for the cases without SBLI and the weakest impinging shock cases. Various wedge angle degrees were to yield SBLI conditions ranging from fully attached to separated flow. The experiments reasonably captured both the flutter boundary and the post-flutter oscillations. However, as the strength of the incident shock increases, the reduced-order models fail to capture the post-flutter response.

The scope of the present work is to perform high-fidelity simulations based on very high-order (11th-order) accurate implicit Large Eddy Simulations (ILES) for various cases relevant to AFRL's experiments. To date, we have investigated the effects of static surface curvature/deformation on the mean and fluctuating components of the surface pressure for a separated SBLI case, e.g., the RC-19 configuration with the 12deg wedge. Currently, simulations for the unsteady surface deformation cases on the separated SBLI loads (using prescribed motions) are being carried out.

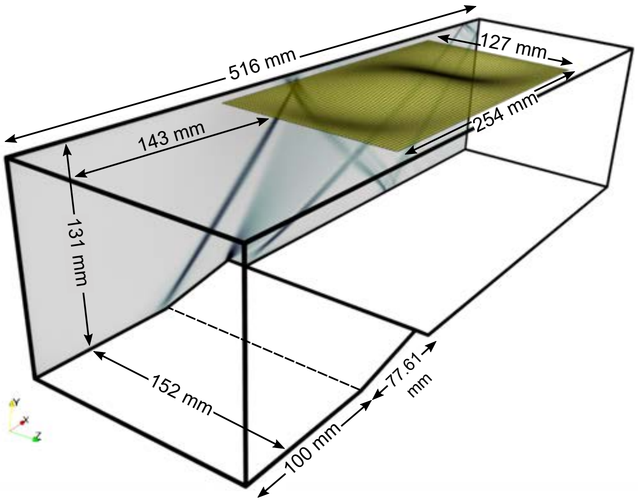

FIG. 14. Schematic of the computational domain considered.

TABLE II. Flow properties at the RC-19 inlet

δ_0 (mm)	U_∞ (m/s)	p_∞ (kPa)	ρ_∞ (kg/m^3)	T_∞ (K)
4.74	579	48.4	0.76	221.9

A schematic of the RC-19 computational domain is given in Fig. 14, and the inflow conditions prescribed are summarized in Table II.

VI. DISCUSSION

A. Planar panel (no deformation)

Initially, the case without deformation was considered to assess various computational methods and ascertain the desired mesh resolution. A digital filter/synthetic turbulence boundary condition was employed at the inlet to create the required supersonic turbulent boundary layer. The remaining boundary conditions are supersonic outflow at the outlet, viscous (no-slip) walls at the upper and lower surfaces, and periodic conditions on the spanwise sides.

1. *Grid sensitivity study*

Before the investigation of the deformation cases, a grid sensitivity study is carried out on a flat panel case to identify the most optimum grid size required to capture the main quantities of interest, i.e., the mean and root-mean-square (RMS) pressure, particularly in the vicinity of the SBLI. Both of these quantities play a deciding role in the overall deformation of the compliant panel. While the mean pressure exerts a force per unit area over the surface, which is significant at the SBLI region due to the oblique shock wave impingement, the RMS pressure results in an (aero-)acoustic loading, which is typically measured in the sound pressure level –otherwise known as the decibel (dB) scale– calculated according to $\mathrm{L_p} = 20\log_{10}(p_{\mathrm{rms}}/p_0)$, where the reference sound pressure is equal to $p_0 = 20\,\mu$Pa.

Mesh resolution recommendations for LES and DNS simulations are covered in the literature extensively[130–132]. A typical fine mesh for conducting wall-resolved LES requires a $\Delta x^+ \approx 50 \sim 130$, and a $\Delta z^+ \approx 15 \sim 30$. To resolve the TBL, about $n_y^w \approx 10 \sim 30$ points are required within the TBL height (or thickness δ), with the first point ideally placed at a distance of no more than $\sim$1 to capture the linear (laminar) sublayer. The mesh is clustered only in the vertical wall-normal direction, whereas equidistant grid spacing is used in the streamwise (x) and spanwise (z) directions. The number of mesh

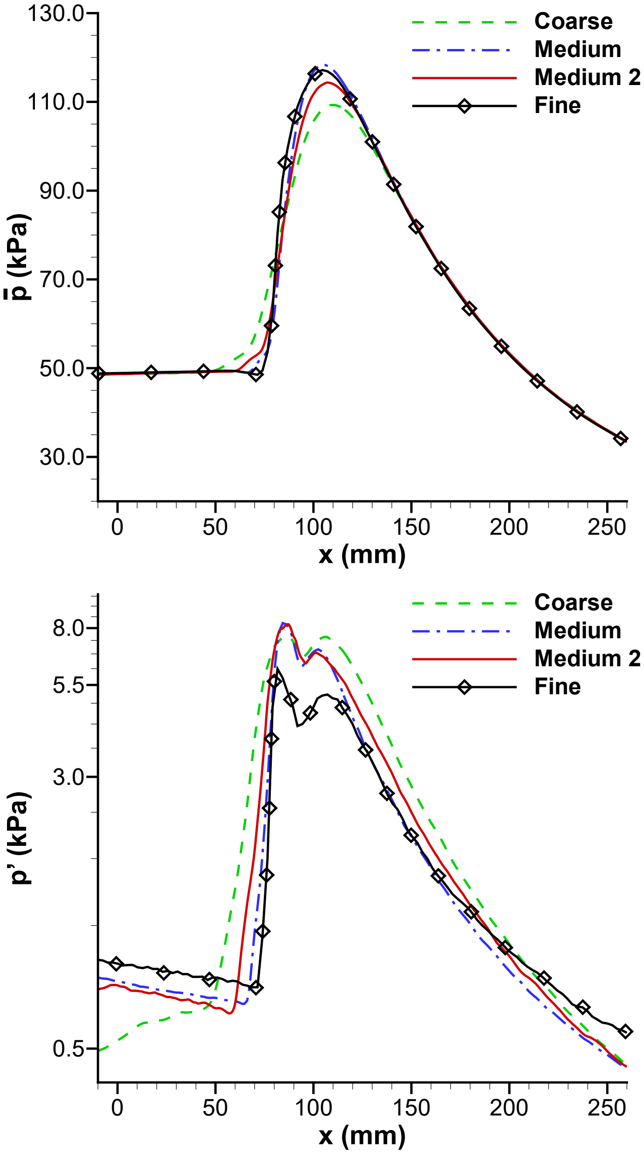

FIG. 15. Grid convergence of the (a) mean pressure, top, and (b) RMS pressure, bottom, profiles along the planar thin panel.

points and corresponding mesh spacing are summarized in Table III along with the LES and DNS recommendations from the literature. The present mesh spacing (Δy) is scaled using the conventional inner variable method $\Delta y^+ = u_\tau \Delta y / \nu_w$, where $u_\tau = \sqrt{\tau_w / \rho_w}$ is the friction velocity, ν_w, τ_w and ρ_w are the near-wall kinematic viscosity, wall shear-stress, and density, respectively.

The grid convergence study used a flat surface (no deformation). Thus, the turbulent flow in the spanwise direction becomes homogeneous. This allows for a shorter spanwise length to be used. Thus, a width of $L_z = 33$ mm ($\approx 7\delta_0$) was used for the coarse, medium, and fine grids, in contrast to the medium 2 grid where the full wind tunnel width of $L_z = 152$ mm was used. In all cases, the clustering of the wall-normal cells followed an expansion ratio of $\sim 1.1 \pm 0.02$.

TABLE III. Mesh parameters of the present ILES; mesh size given in the number of cells (N_c).

Mesh	n_x	n_z	n_y	Δx^+	Δz^+	y^+	N_c
Coarse	256	32	128	1,076	551	4.8	1,048,576
Medium 1	576	64	196	478	275	4.8	7,225,344
Medium 2	384	128	192	717	634	4.8	9,437,184
Fine	1,026	176	220	268	100	2.7	39,726,720

For the coarse mesh, the incoming boundary layer height was discretized by $n_y^w = 28$ points, for the medium and medium 2 meshes 42 and 37 points, respectively, and for the fine mesh 42 points. Thus, the wall-normal resolution within the TBL remains adequate in all cases.

Note that a fine wall-resolved ILES simulation would require reducing the mesh cell sizes in the x and z directions to a third, thus increasing the computational cost by almost an order of magnitude. Further accounting for the full wind tunnel width of 152 mm –versus the narrower 33 mm domain width increases the computational cost by an additional ~4.6 times. The resulting computational cost would thus be ~175 times greater compared to the medium two mesh employed, making it substantially more difficult – if not impossible– to carry out the present parametric study within a reasonable time frame.

Both the mean and RMS pressure obtained using several grids of increasing size are plotted in Fig. 15 (a) and (b), respectively. The values of both quantities of interest can be seen to converge gradually. The medium mesh 2 gave a reasonable agreement to the much finer mesh and was, therefore, selected to carry out the present parametric study. Henceforth, the planar panel results on the medium 2 mesh will be referred to and labeled as "$M0$".

Finally, another important parameter is the size of the resolved separation bubble that forms between the impinging and separated shock waves at the SBLI. Figure 16 demon-

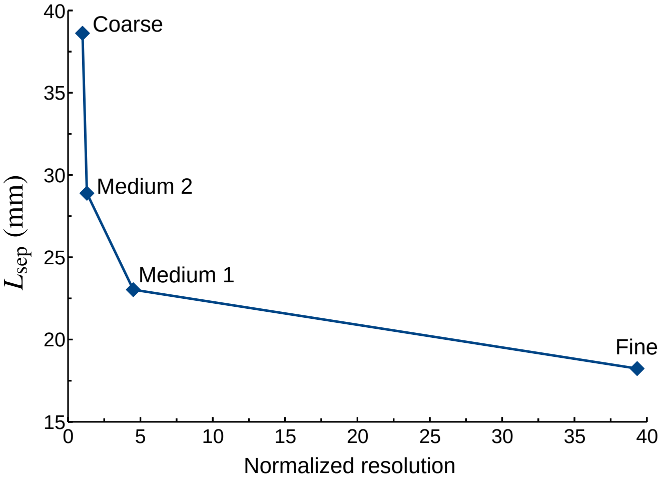

FIG. 16. Effect of the (near wall) mesh resolution on the obtained size of the recirculation bubble, L_{sep}; mesh resolution index, $1/\left(\Delta x^+ \times \Delta z^+ \times y^+\right)$, normalized by the coarse mesh.

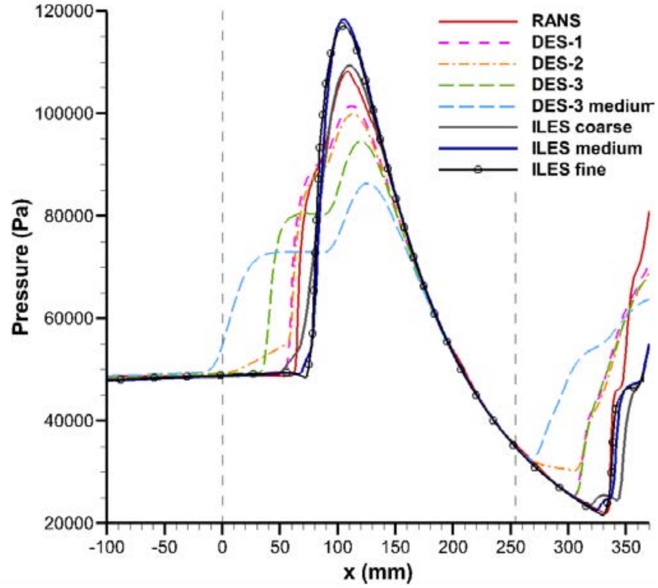

FIG. 17. Comparison of the mean pressure profile along the compliant panel using different numerical methods and mesh resolutions.

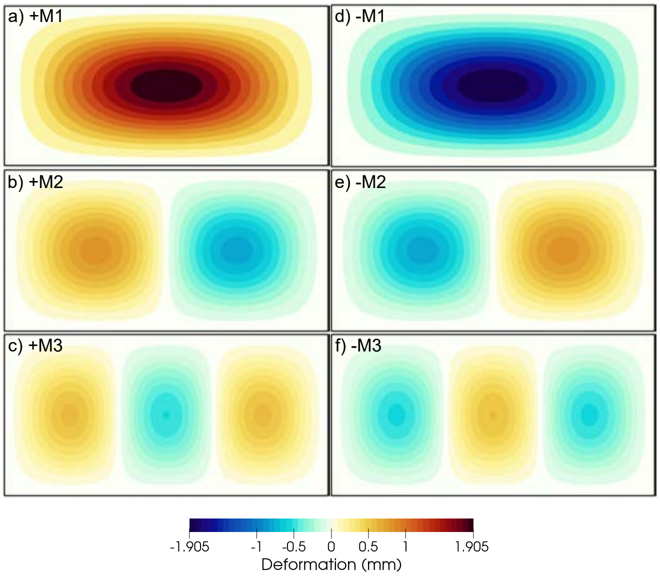

FIG. 18. Compliant panel static (permanent) deformation modes examined.

strates that L_{sep} has not fully converged yet. For the Medium 1 mesh, L_{sep} is approximately 1.25 times larger than the Fine mesh, while for the Medium 2 mesh, it is 1.6 times larger. It should be noted that the Medium 1 and 2 meshes use the same y^+ value at the wall. Therefore, the difference in the resolved L_{sep} must be attributed to the lower streamwise and spanwise resolutions (see Table III for a comparison).

2. *Investigation of numerical methods accuracy*

Figure 17 shows that the RANS (Spalart-Allmaras model) reasonably predicted the mean surface pressure. However, the maximum value was under-predicted around the panel or over-predicted post the compliant panel. The results are compared with the finest ILES simulation.

Moreover, different detached eddy simulations (DES) methods revealed that the hybrid RANS-LES approach is unsuitable for the present case. On the other hand, ILES showed promising results even on a very coarse mesh examined (∼0.5 million cells). Using the high-order methods available, i.e., 11th-order WENO in space and 4th-order Runge-Kutta in time, the results obtained on the medium grid (∼7.2 million cells) already showed signs of (grid) convergence compared to the fine grid (∼40 million cells). The details of the meshes used in the grid convergence study are given in Table III.

The grid convergence and numerical methods studies demonstrate that the medium mesh offers the best ratio between accuracy and computational cost. In a coarse-grained simulation (CGS), large energy-containing structures are resolved, smaller structures are spatially filtered out, whereas unresolved subgrid-scale (SGS) effects are modeled[60]. CGS includes classical large eddy simulation (LES) strategies employing an explicit SGS model or implicit LES (ILES) relying on SGS modeling and filtering provided by physics-capturing numerical algorithms, i.e., shock-capturing schemes typically employed in finite volume methods. Understanding of this so-called spectral gap, or scale separation, between the large (integral) and the small (viscous) turbulence scales has further improved over the last decade, particularly about CGS modeling[61]. The CGS strategy of separating the resolved from the unresolved scales and modeling the physics effects of the latter constitutes a viable intermediate approach between DNS and RANS to address practical geometries and multiphysics.

B. Static panel deformation

Six cases were chosen for the static deformation so a parametric study could be carried out. Specifically, the parametric studies can be categorized according to two parameters. First, whether the first deformation "bump" is inward (+ve mode) or outward (-ve mode) of the flow, and second, based on the number of "bumps" present. For example, +M2 refers to a case with two surface bumps: inward to the flow and outward. A schematic in Fig. 19 and a surface contour plot in Fig. 18 illustrate the six modes considered.

Second, considering the deformation magnitude of the bumps should be equal in each mode but differ per mode. The location of the peak surface deformation relative to the incoming supersonic turbulent boundary layer (TBL) height is given in Fig. 20. With the single bump, the first mode (±M1) has the largest deformation magnitude within the TBL outer layer. The surface deformation magnitude of the remaining two modes is still relatively large, reaching the upper log-law region in both cases.

The surface deformation modes examined can be mathe-

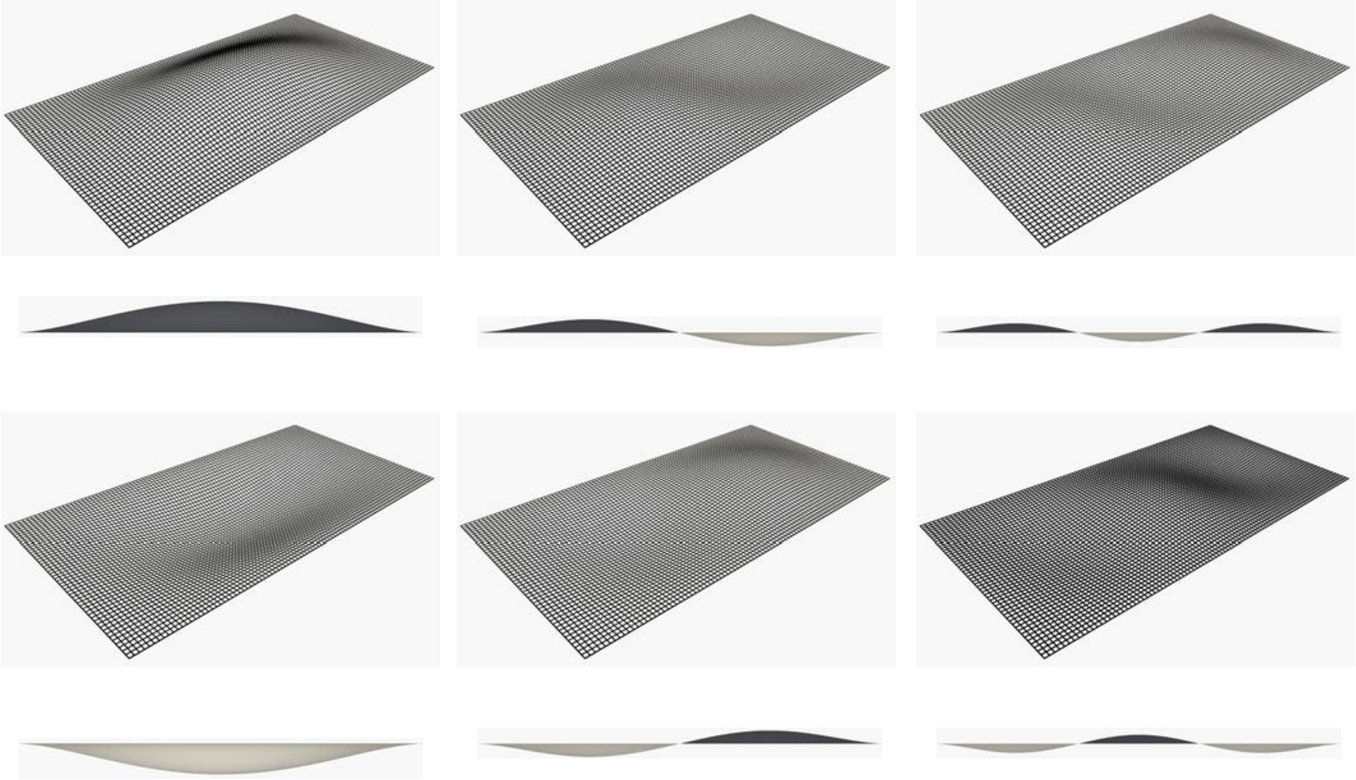

FIG. 19. Modes of deformation considered; rows: first +ve, second -ve; columns: modes 1, 2, and 3.

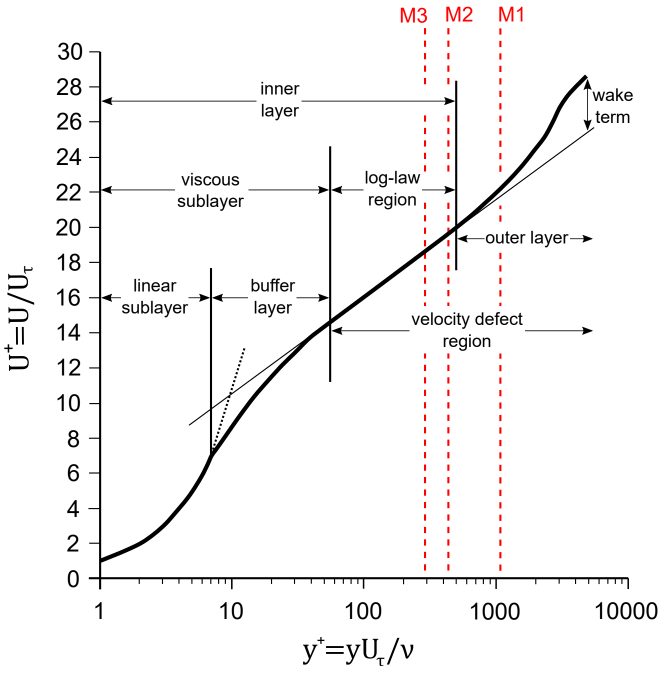

FIG. 20. Peak magnitude deformation relative to incoming TBL.

matically described according to:

$$d_{n_{\mathrm{M}}}(x,z) \simeq a_{n_{\mathrm{M}}} \sin\left(n_{\mathrm{M}}\,\pi \frac{x}{L_{x,p}}\right) \sin\left(\pi \frac{z}{L_{z,p}}\right) \tag{31}$$

Mode	±1	±2	±3
$\max\lvert y\rvert/\delta_0\ (y^+)$ Mach number	0.402 (1017) 1.55	0.17 (428) 1.35	0.114 (290) 1.23

TABLE IV. Compliant panel maximum deformation height and corresponding undisturbed incoming flow Mach number.

for $x \in [0, L_{z,p}]$ and $z \in [0, L_{z_p}]$ are the coordinates within the compliant panel and $a_{n_{\mathrm{M}}}$ is the maximum surface deformation amplitude of the mode number n_{M} (see Table IV). The above equation deviates slightly from the examined modes only near the edges of the clumped thin panel, where the deformation rate is somewhat more gradual and smoother.

Modes ±1–3 were the most dominant modes in the thin panel responses for the $\theta = 12$ deg wedge shock generator. The amplitude for mode 1 was selected to provide a peak deformation equivalent to the max/min measured deformation from the experiments[39,44]. The amplitudes for modes 2 and 3 were scaled so that the surface curvatures were similar for all three modes.

To investigate the static deformation cases, the full spanwise length of the RC-19 wind tunnel had to be employed, increasing the computational requirements by ∼4.5 times relative to the no-deformation case (narrower spanwise computational domain) for the same flow resolution. The "Medium 2" mesh employed comprised of ∼9.5 million cells (details given in Table III). Moreover, the spanwise sides' boundary condition was changed to symmetry/reflection (inviscid wall), as resolving the turbulent boundary layer along the side wall surfaces would have been prohibitively expensive computationally.

The wall surface data was sampled at a time interval of $dt_s \simeq 1.58\ \mu$sec and over a time window of at least $T_s \geq 0.01$ sec for all cases. This ensures that the lowest obtained frequency (T_s^{-1}) is equal to, or less than, 100 Hz, while the highest is equal to the Nyquist frequency (or half the sampling frequency), i.e., $dt_s^{-1}/2 \approx 316$ kHz. The aforementioned frequency was identified as the lowest unsteady deformation mode of the compliant panel during the RC-19 experiments.[39,44,57] Note that all of the power-spectra results herein have been calculated using the discreet fast-Fourier transforms obtained via the FFTW3 library[133].

1. Mean pressure loading response

Figure 21 shows the obtained mean surface pressure along the mid-span of the compliant panel, i.e., where the deformation is largest. The -ve modes cause a decrease in the mean pressure loading at the front of the compliant panel, whereas the +ve modes cause an increase. Further downstream, the interaction between the incident shock wave, the SBLI, and the various surface modes results in a complex behavior of the mean pressure. Overall, the maximum mean pressure at the SBLI is found to vary around a maximum of around 10% between the various modes.

In the post-SBLI region, from ~130 mm to ~190 mm, the mean pressure response appears opposite to the SBLI region. For example, in the case of mode +1, the mean pressure is increased –relative to the planar case– but decreases after that. The exact opposite process occurs for the -1 mode. The only exception appears to be both ±2 modes, which appear to converge towards the planar case (M0) mean pressure.

Near the end of the compliant panel, at 254 mm, the ±1 modes do not depart from their post-SBLI behaviour. Modes ±2 show a change downstream of ~180 mm, whereas modes ±3 from around 200 mm, both likely due to the panel deformation gradient sign change that occurs at said locations.

The spatial distribution of the near wall mean pressure, $\bar{p_w}$, near the surface is given in Fig. 22. The initial and clear response of the pressure at the "front" of the compliant panel depending on the mode sign is evident. It is immediately apparent that any differences compared to the planar case are symmetrical about the midspan. This is not unexpected since the deformation modes are also symmetrical about the midspan. However, it does reveal that (a) no mean flow asymmetries are caused, and (b) the sample size used to obtain the means was sufficient.

Interestingly, the results reveal that the spanwise location of the peak (mean) pressure at the SBLI region (dark red colour) changes depending on the mode. The peak values may be located at the mid-span (the mode -M2), at the sides (modes: +M2 and +M3), or approximately equal along the entire span (modes ±M1).

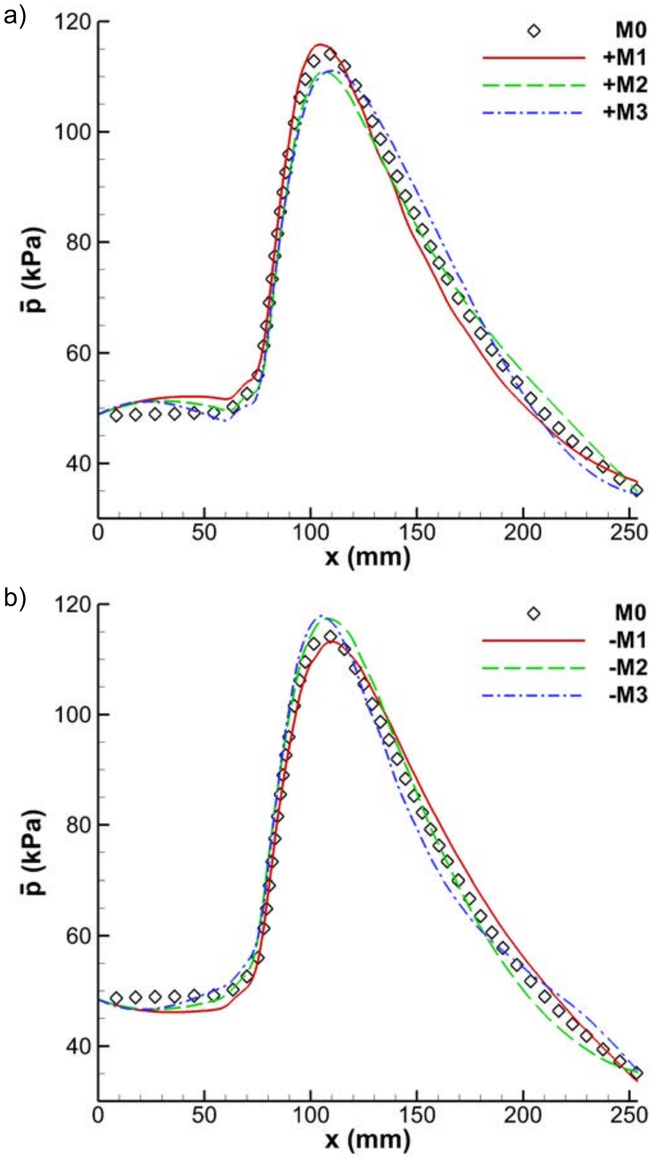

FIG. 21. Mean pressure profiles along the mid-span of the compliant panel in the streamwise directions.

Foremost, the surface deformation modes cause a change in the mean pressure about the midspan. In addition, however, Fig. 21 reveals that the extent of the area over which the initial mean pressure change occurs greatly reduces with increasing deformation mode. This is attributed to the decrease in the deformation wavelength with increasing mode number, as per Eq. (31).

At the oblique shock impingement region, noticeable by the high mean pressure (red colored contours), the surface deformation modes +1, -2, and -3 have a positive streamwise gradient, i.e., the surface is moving towards the flow, and vice-versa for their mirror modes. The positive streamwise deformation gradient results in an increase in peak mean pressure at the SBLI, whereas their mirror modes result in a decrease. For the ±1 modes, the mean pressure change is more consistent along the spanwise direction, whereas for ± modes 2 & 3, it is more centered at the midspan. Either way, the change in

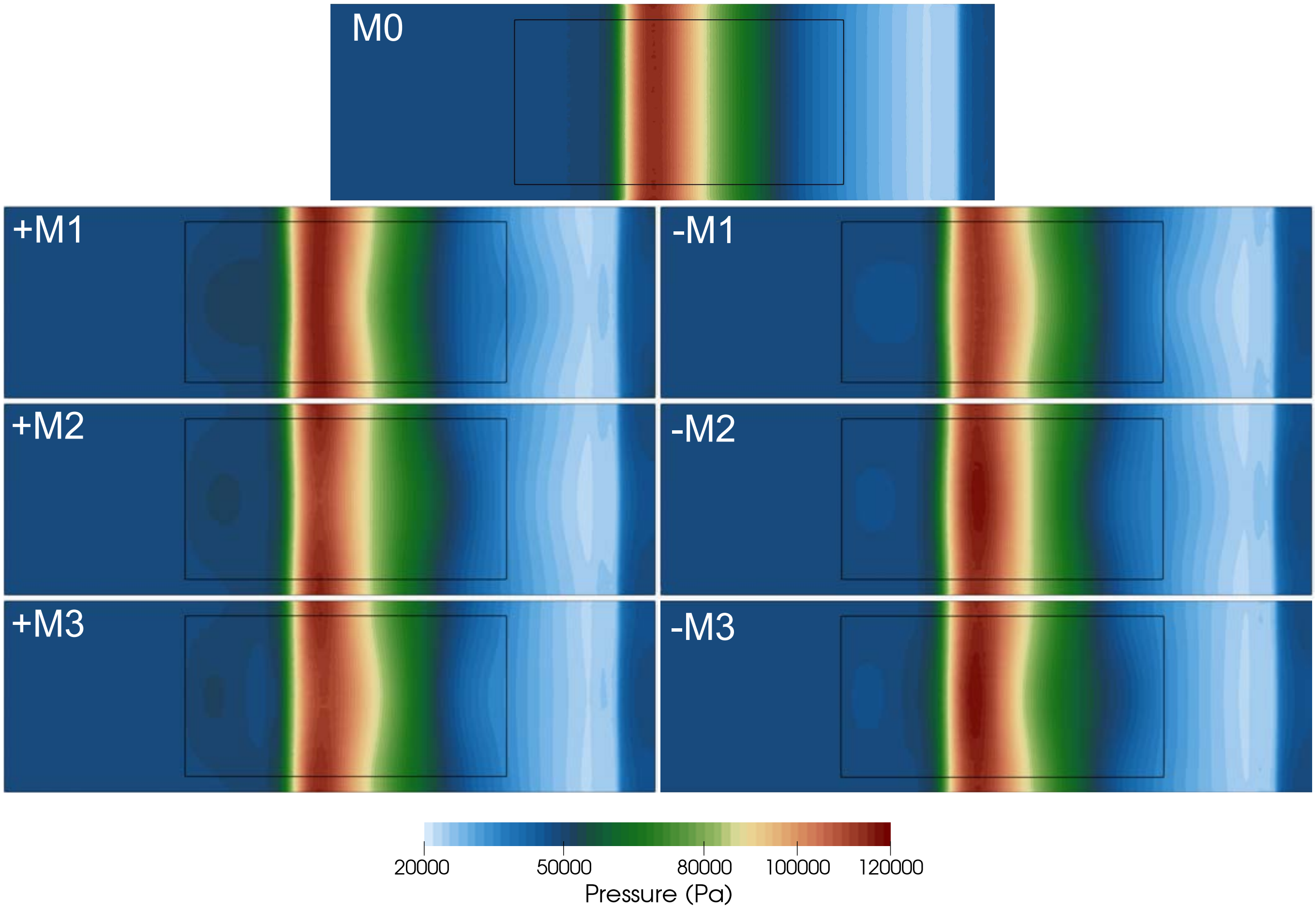

FIG. 22. Mean pressure at $y^+ = 5$; solid black line illustrates the compliant panel outer boundary.

peak mean pressure at the SBLI is around $\sim \pm 10\%$ compared to the planar case.

As noted earlier, Fig. 22 further shows that the mean pressure contours attain a spanwise curvature, which is symmetrical about midspan as expected. The spanwise curvature can be either concave or convex, depending on the deformation mode and the streamwise location. Interestingly, the frontal region of the SBLI appears to be less affected by any of the imposed surface curvatures and appears smooth compared to anywhere else along the compliant panel. The underlying mechanism responsible is not evident and warrants further careful examination.

2. *Acoustic loading response*

Figure 23 plots the sound pressure level (SPL) in units of decibels (dB) at and around the compliant panel. For all cases, the SPL at the undisturbed TBL and before the panel is around 150 dB. At the relaxation region, post the SBLI and the panel, the SPL drops in the region of 140 dB due to the Prandtl–Meyer expansion fan that forms at the aft of the wedge shock generator located at the opposite wall, as per Fig 14. No change in the minimum nor maximum values of the SPL is observed, even at the SBLI. Similar, however, to the mean pressure wall surface distribution, $\bar{p}_w(x,z)$, the SPL also exhibits a considerable spanwise "bending", which is symmetric about the midspan, shortly after the SBLI –as evident by the white/yellow contour regions at the right half of the panel. This is particularly prominent in the $\pm M1$ and $\pm M3$ modes, but less so for the $\pm M2$ modes whose spanwise SPL distribution remains relatively flat, in contrast to the response of the mean pressure. The SPL at the SBLI remains relatively similar across modes, apart from a very small but noticeable spanwise bending. This suggests that the imposed surface deformations examined are insufficient to cause any meaningful effect on the SPL generated by the SBLI.

Figure 24 plots the normalized pre-multiplied pressure power spectrum using local scaling (Φ_n) for the planar case as well as the six deformation modes considered, which is defined as:

$$\Phi_n(x,f) = \Phi(x,f) \; / \; \Phi_s(x) \tag{32}$$

where $\Phi(x,f) = f\,\mathcal{P}(x,f)$, $\Phi_s(x) = \int \mathcal{P}(x,f)\,\mathrm{d}f$, and $\mathcal{P}(x,f)$ is the pressure power-spectrum. The normalized pre-multiplied pressure power spectrum (Φ_n) shows the frequencies that contribute locally to the energy of the signal and

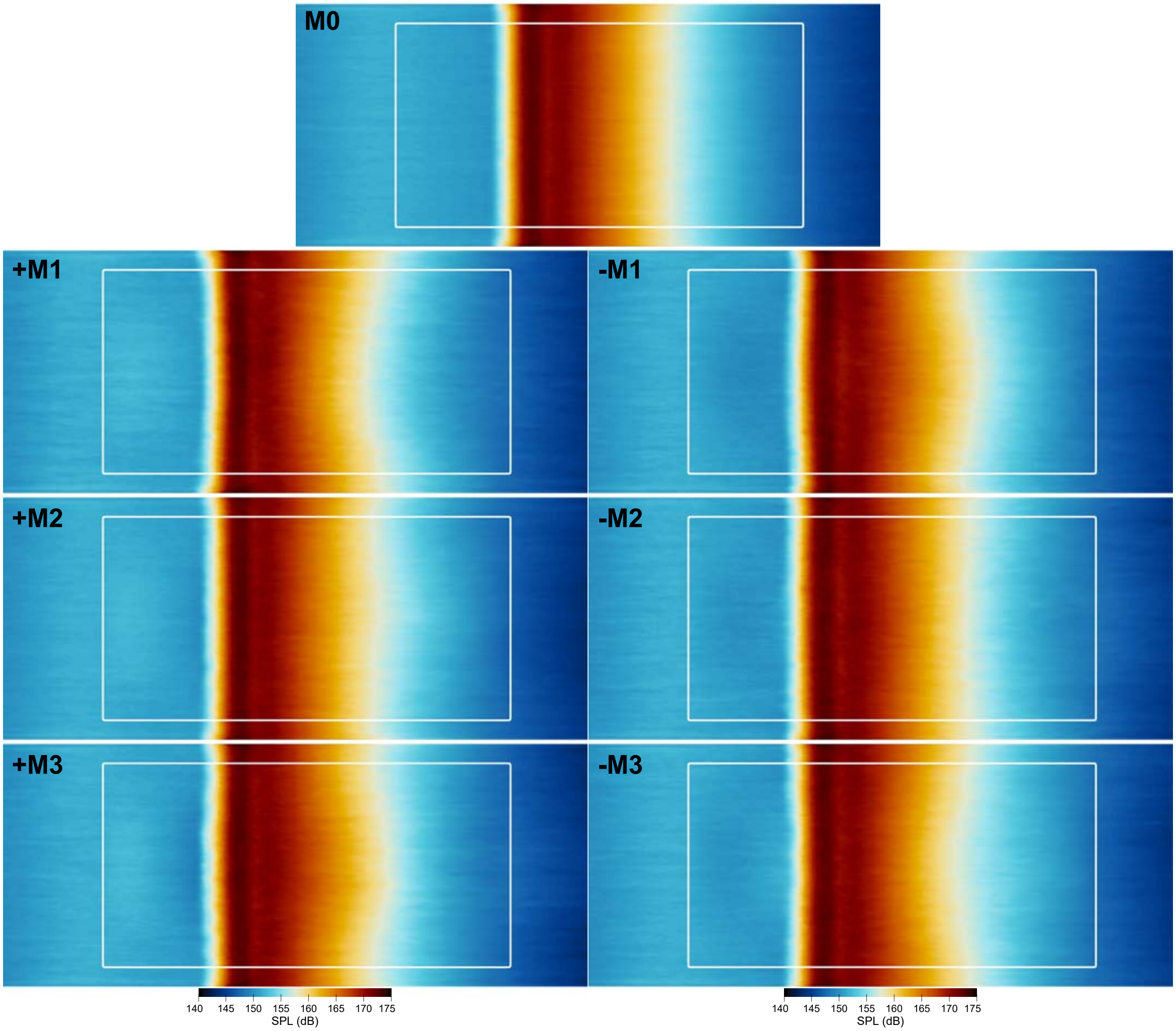

FIG. 23. Sound pressure level (SPL) in decibels (dB) at the surface of the planar and six statically deformation modes examined. The rectangular rectangular region enclosed within the white solid line indicates the compliant panel region.

is particularly useful in revealing the position of the low-frequency oscillation associated with the λ-shock foot's recirculation bubble that forms at the SBLI. Before the SBLI, Φ_n is largest at $f \simeq 20 - 100$ kHz. This frequency range is in the same order as the TBL's characteristic frequency ($U_\infty/\delta_0 \simeq 63.5$ kHz), about which the maximum is located. At the SBLI, Φ_n peaks between the 3–4 kHz range, though the pressure fluctuation energy can be seen to begin to rise from at least as low as 100 Hz. Like Bernardini et al.[134], the low-frequency peak is widespread along a broad range of frequencies, suggesting an underlying shock unsteadiness more complicated than just a simple periodic oscillation.

In large upstream Mach number SBLI, the separation point and the reflected shock foot are well known to oscillate in the streamwise direction at a frequency much lower than the inverse of the characteristic travel time over the separation bubble length L_{sep}. The corresponding dimensionless frequency, or Strouhal number, $St_{L_{\mathrm{sep}}} = fL_{\mathrm{sep}}/U_\infty$ is thus small and lies in the range $0.02 - 0.06$[28,135,136], though, larger values have also been mentioned in the literature, e.g., of $St_{L_{\mathrm{sep}}} \simeq 0.08$[137]. For the present coarse-grained ILES data, the distance between the separation and re-attachment of the detached TBL at the SBLI is $L_{\mathrm{sep}} \simeq 27$ mm (or $L_{\mathrm{sep}} \simeq 5.7\delta_0$), resulting in a dimensionless low-frequency shock oscillation of $St_{L_{\mathrm{sep}}} \simeq 0.14$, which is a little over twice the upper expected value. However, it should be noted that the unscaled pressure $\mathcal{P}$ shown in Fig. 25, shows the highest values to be attained circa 200–400 Hz, corresponding to $St_{L_{\mathrm{sep}}} \simeq 0.01 - -0.02$, much closer to

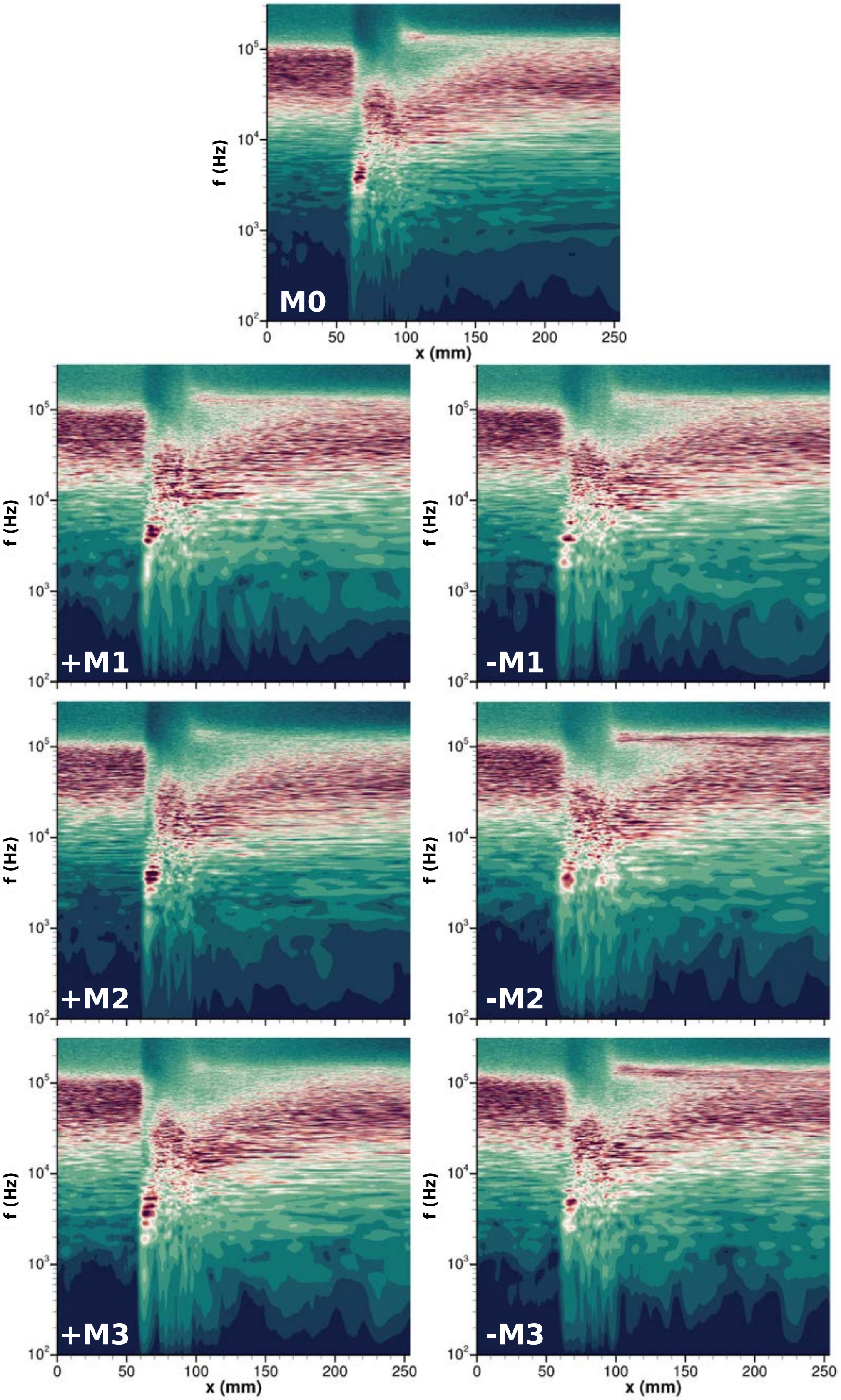

FIG. 24. Spectrogram of the normalized pre-multiplied pressure power-spectrum, $\Phi_n = f\mathcal{P}(x,f)/\int\mathcal{P}(x,f)\,\mathrm{d}f$, along the compliant panel midspan.

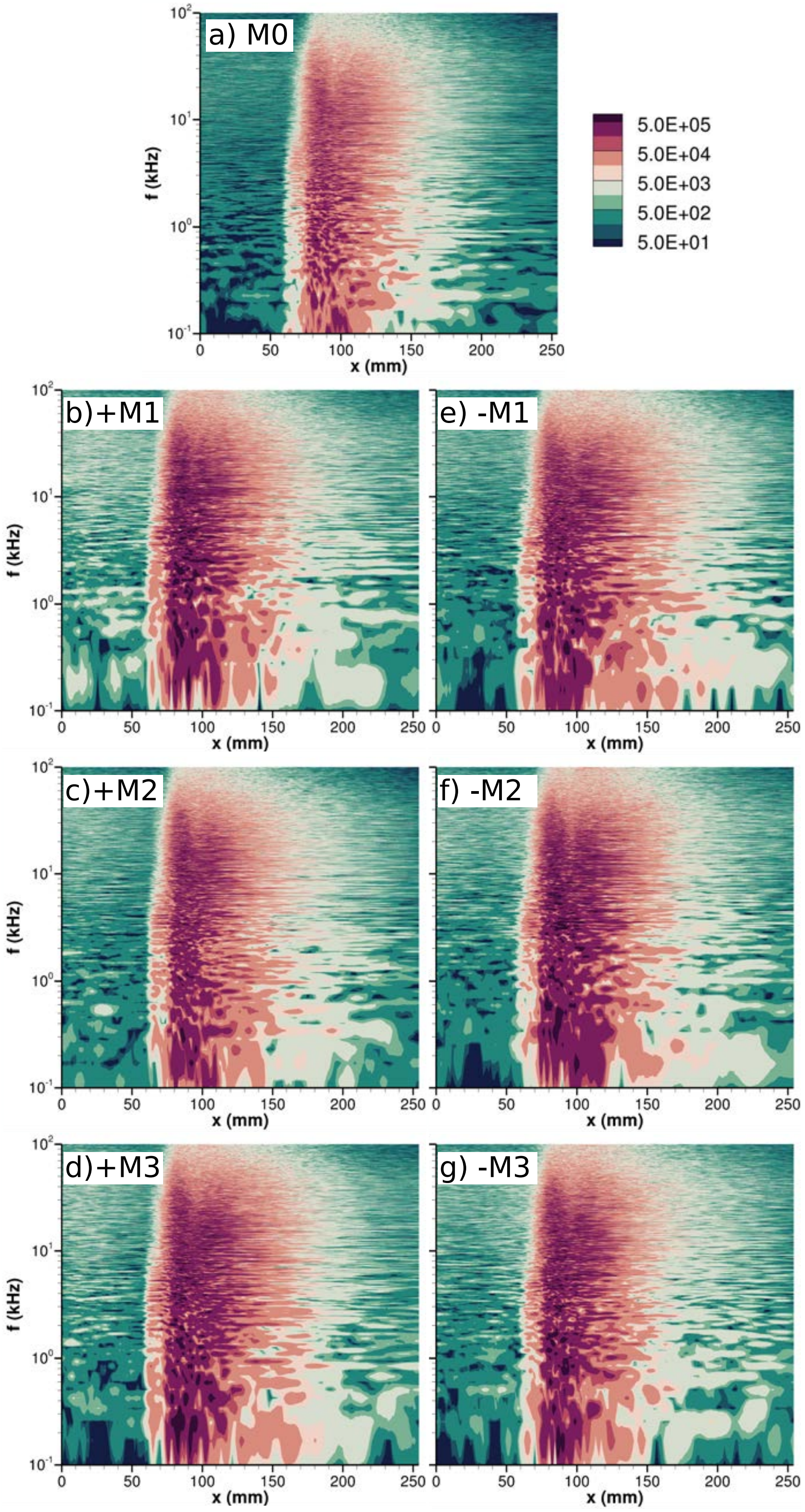

FIG. 25. Spectrogram of the pressure power-spectrum, $\mathcal{P}(x, f)$, in the streamwise $(x-)$ direction along the compliant panel midspan; frequency (y-axis) in log-scale for $f \in [0.1, 100]$ kHz; $\mathcal{P}$ in units of Pa^2.

the expected range. Barring any specific case or set-up peculiarities unaccounted for, the discrepancy might be attributed to the coarse-grained ILES over-predicting the recirculation bubble size L_{sep}, and/or under-predicting the strength of the low-frequency oscillation. In wall-resolved LES, either quantities can be affected by insufficient mesh resolution. Thus, the resolved low-frequency unsteady shock motion of the reflected shock, $St_{L_{\text{sep}}}$, can be sensitive to the near wall mesh resolution, which can be verified using a finer grid resolution. Indeed, Fig. 16 in section § VI A 1 showed that L_{sep} for the Medium 2 mesh was approximately 1.6 times larger than that obtained on the fine mesh.

The normalized pre-multiplied pressure power spectrum can also help define the present test case's low-, mid-, and high-frequency regions. The undisturbed and re-attached TBLs are in the 10–100 kHz mid-frequency bandwidth. Thus, below 10 kHz can be considered the low-frequency domain (where the shock breathing motion is located), while above 100 kHz is the high-frequency domain.

Except for the -$M2$ and -$M3$ modes, all other modes enhance Φ_n at the low-frequency domain relative to the planar case. As for the planar case, the low-frequency oscillation for mode -$M1$ appears to commence at just over 2 kHz instead of at 3 kHz, though it appears to be more "fragmented". The positive +$M1$ mode seems to mildly enhance Φ_n in the 1.5–2.5 kHz range, while mode +$M2$ at around 1.5 kHz. Mode +$M3$ appears to affect the low-frequency Φ_n the most, causing a moderate enhancement at 800 and 2,000 Hz, separately. Generally, the low-frequency unsteady pressure hotspot at $\sim$4 kHz appears to be strengthened by the positive deformation modes, whereas weakened by the negative modes. This can be largely attributed to the interaction between the compression waves produced at the fore of the recirculation bubble –which form the separation shock– with the compression or expansion waves produced upstream due to the positive or negative surface inclination, respectively.

In all cases, the SBLI λ-shock wave's recirculation bubble has been re-attached by $x \simeq 100$ mm. Between the TBL detachment and re-attachment, there are clear indications of three separate low-frequency unsteady pressure enhancement regions. The first corresponds to the low-frequency motion of the λ-shock wave already discussed above. The second appears to be located in the middle of the recirculation bubble, while the third is associated –due to its proximity– to the separated TBL re-attachment location. This suggests a very complex behavior of the recirculation bubble, which is present in all modes examined.

Shortly after, at $x \approx 110$ mm, the locally normalized pre-multiplied pressure power spectrum, Φ_n, is characterized by a secondary high-frequency peak, which occurs at $f \simeq 150$ kHz and extends downstream, where at $x \approx 160$ mm it merges with the large Φ_n formed by the developing re-attached TBL. The latter peaks between 30-40 kHz, lower than the undisturbed TBL's 30-100 kHz range. The Φ_n in the relaxation region appears similar to the planar case. However, the secondary high-frequency peak at $(x, f) = (110\,\text{mm}, 150\,\text{kHz})$, though still present in all cases, is found to vary in strength. Relative to the planar case ($M0$), modes -$M2$ and -$M3$ appear to enhance it, modes +$M2$ and +$M3$ suppress it, while modes $\pm M1$ neither. The response appears to match the local surface inclination. Where the surface inclination is negative (-$M2$ and -$M3$) at $x \simeq 110$ mm, the high-frequency Φ_n at $f \simeq 150$ kHz is enhanced, while where it is positive (+$M2$ and +$M3$) it is suppressed. For modes $\pm M1$, the local surface inclination is very small, hence the similarity to the planar case.

Figure 25 shows the pressure power-spectrum, $\mathcal{P}$, contour plots obtained along the midspan of the compliant panel with an emphasis on the frequency domain up to 100 kHz. Moving along the streamwise direction, it becomes evident that several static deformation modes increase the pressure $\mathcal{P}$ even before the SBLI onset ($x \lesssim 60$ mm). Specifically, below a $\sim$1 kHz frequency, modes +$M1$ and +$M2$ increase $\mathcal{P}$. According to Fig. 18, said modes (+$M1$ and +$M2$) are the only –of the examined cases– with a substantial positive surface inclination before the SBLI onset. As a result, a compression wave is generated before the SBLI, which is thought to be the leading factor behind the observed low-frequency enhancement. In contrast, the negative modes cause an expansion fan to form, which generally attenuates flow unsteadiness. Consequently, the negative modes, particularly -$M1$ and -$M2$, attenuate $\mathcal{P}$ in the sub 1 kHz range relative to the planar case (mode M0).

Above $\sim$1 kHz and pre-SBLI still ($x \lesssim 60$ mm), all positive modes generally amplify $\mathcal{P}$ relative to the planar case, with mode +$M2$ showing the weakest response. On the other hand, the negative modes do not cause any significant changes, particularly mode -$M1$. Modes -$M2$ & -$M3$ show a relatively weak increase in the high-frequency domain of $\mathcal{P}$, somewhat similar to the +$M2$ mode.

At the SBLI ($60 \lesssim x \lesssim 160$ mm), all of the compliant panel deformation modes amplify the pressure power spectrum relative to the planar mode, as evidenced by the darker and more extensive red-coloured (higher value) regions shown in Fig. 25. The above occurs irrespective of the sign of the deformation modes' surface inclination pre-SBLI. The latter determines whether a compression or expansion wave is formed before the SBLI, which will enhance or attenuate the oblique shock wave, respectively, before it impinges onto the surface.

In the SBLI region, mode +$M2$ enhances the pressure $\mathcal{P}$ the least relative to the planar panel case. This is attributed to mode +$M2$ having the largest negative deformation rate within the SBLI. Overall, the increased $\mathcal{P}$ cannot be attributed to either the deformation or the deformation rate alone, suggesting that a correlation between the two does not exist or is not dominant. This suggests, more likely than not, that the flow response is more complex and not limited to just a single parameter. For example, if the surface deformation rate within the SBLI region was critical, then modes $\pm M1$ and $\pm M3$ should show a smaller response since it remains comparatively low. Yet, the pressure $\mathcal{P}$ in the aforementioned modes is still enhanced. Furthermore, despite modes $\pm M2$ being the only ones to have a constant sign of deformation rate throughout most of the SBLI region, they exhibit vastly different responses in $\mathcal{P}$. In conclusion, all of the surface deformation modes examined lead to an increase in the pressure $\mathcal{P}$, with mode +$M2$ being the sole outlier to the rule. The latter can only be attributed to mode +$M2$ tightly containing the entire recirculation bubble within its depressed surface, as indicated in Fig. 18.

Post SBLI, and towards the end of the compliant panel ($x \gtrsim 160$ mm), Fig. 25 reveals that all deformation modes exhibit an increased pressure $\mathcal{P}$ relative to the planar panel case (mode M0). However, a closer inspection of the low-frequency pressure power-spectrum ($\mathcal{P}$) content in Fig. 25 reveals that the initial enhancement occurs at a different frequency. Specifically, the deformation modes $+M1$, $-M2$, and $+M3$ show that the initial rise in $\mathcal{P}$ occurs in the $\sim 0.1-0.3$ kHz frequency bandwidth, whereas that of the remaining three modes, namely $-M1$, $+M2$, and $-M3$, slightly higher in the $\sim 0.2-0.4$ kHz frequency bandwidth. A common feature evident in the above mode groupings is the streamwise deformation rate at the end of the buckled plate, per Fig. 18). The amplification of $\mathcal{P}$ for the former frequency range ($0.1-0.3$ kHz) occurs for the deformation modes whose panel surface is inclined negatively (buckled outwards of the flow), whereas, for those belonging to the latter frequency range ($0.2-0.4$ kHz), the panel surface is inclined positively (buckled inwards towards the flow).

C. Time varying panel deformation

In the previous section, the effect of different statically deformed panel shapes, typically encountered and observed in wind-tunnel experiments, on the response of the acoustic loading was examined. In the present section, the response of the acoustic loading will be assessed with respect to a moving/vibrating panel surface, approximating the observations in the experiments. Experimental measurements of the compliant panel deformation in time will be utilized in the coarse-grain ILES.

Figure 26 compares the buckled compliant panel surface for the unsteady deformation modes vs the static $+M3$ mode. The latter is chosen for reference and comparison since it exhibits similar surface deformation mode 3, albeit symmetrical –all three unsteady modes are no longer symmetrical in the spanwise direction. Apart from the movement of the surface, all three unsteady modes examined exhibit a larger mean deformation amplitude relative to the static $+M3$ mode, which is a little over double. Unsteady modes case 31 ($C31$) and case 32 ($C32$) appear fairly similar, while case 33 ($C33$) contains instances of positive deformation (deforming into the flow). Note the red solid line along the midspan indicating the region at which all results are presented and the comparisons made.

Moving surface deformation was obtained from the RC-19 experiments and provided as a Matlab data file containing 3 seconds. The coarse-grain ILES simulations were run for a total of 0.03 sec. Statistics were gathered over the time windows 0.002-0.032 s, where the first 0.002 s was omitted for the case to become statistically steady). Thus, the min resolved frequency was over $\sim$33 Hz.

1. Geometric conservation law

To account for the moving surface in the computations, the geometric conservation law (GCL) was implemented. This ensures the flow's mass, momentum and energy conservation as the computational mesh is adapted to the deforming/moving surface(s). As the surface mesh deforms, so do the coordinates of the computational cells vertices. The cells' volume, therefore, changes according to the GCL according to:

$$\frac{\mathrm{d}}{\mathrm{d}t}\iiint_V \mathrm{d}V = \oiint_S \mathbf{v}_S \cdot \mathbf{n}\,\mathrm{d}S \tag{33}$$

where $\mathbf{v}_S = [x_t, y_t, z_t]^T$ is the cells' surface velocity (Lagrangian), which must be accounted for in the solution of the Riemann problem (Eulerian). The cell surface velocity, $\mathbf{v}_S$, is taken equal to the mean of its vertices velocity, which in turn are obtained according to:

$$\frac{\mathrm{d}\mathbf{x}}{\mathrm{d}t} = \frac{\mathrm{d}\mathbf{x}_M}{\mathrm{d}\tau}\frac{\mathrm{d}\tau}{\mathrm{d}t} \tag{34}$$

where $\mathbf{x}_M$ is the interpolated coordinate location from the Matlab file and $\mathrm{d}\tau$ is the time-step size between the two consecutive deformation solutions provided in the Matlab file that enclose the physical time in the CFD simulation. To ensure neighboring cell surfaces do not intersect and/or become entangled, it is necessary to also shift neighboring mesh vertices as appropriate. In the present implementation, this is achieved by ensuring that the relative position of the vertex on its $\imath$ line remains constant per direction, whereas for a structured 3D solver $\imath = [i, j, k]^T$. As the vertices comprising the moving surface boundary set the grid velocity, it gradually diminishes the further away the interior vertices are located until the static (non-moving) domain boundary vertices are reached.

2. Acoustic loading response

Figure 27 plots the sound pressure level (SPL) in units of decibels (dB). A slight increase of 10-15 dB can be observed at the beginning of the three unsteady compliant panel cases. The stronger compression waves mostly cause this due to the steeper and larger mean positive deformation amplitude relative to the static $+M3$ mode. However, as the pressure power-spectrum analysis will later show, the vibrating surface may partly contribute to the overall SPL magnitude. Differences in the topological distribution of the SPL, specifically in the spanwise direction, are now much more pronounced, particularly for the $C31$ and $C32$ cases. Importantly, for these two cases, a larger area of the compliant panel is covered by a higher SPL (>155 dB).

Next, Figure 28 plots the locally normalized pre-multiplied pressure power spectrum. In addition to the low-frequency oscillation between the 1–4 kHz range obtained for the static modes, the unsteady panel deformation cases exhibit a strong(er) response at an even lower frequency, which can be seen across almost the entire panel length. Though the

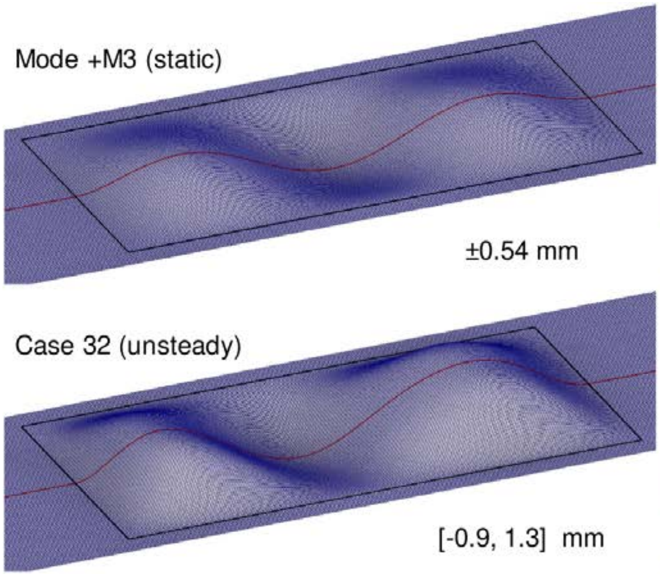

FIG. 26. Comparison of a snapshot of the buckled compliant panel surface for the unsteady deformation modes vs the static +*M*3 mode; the minimum and maximum surface deformation locations are given in the lower left corner of each mode.

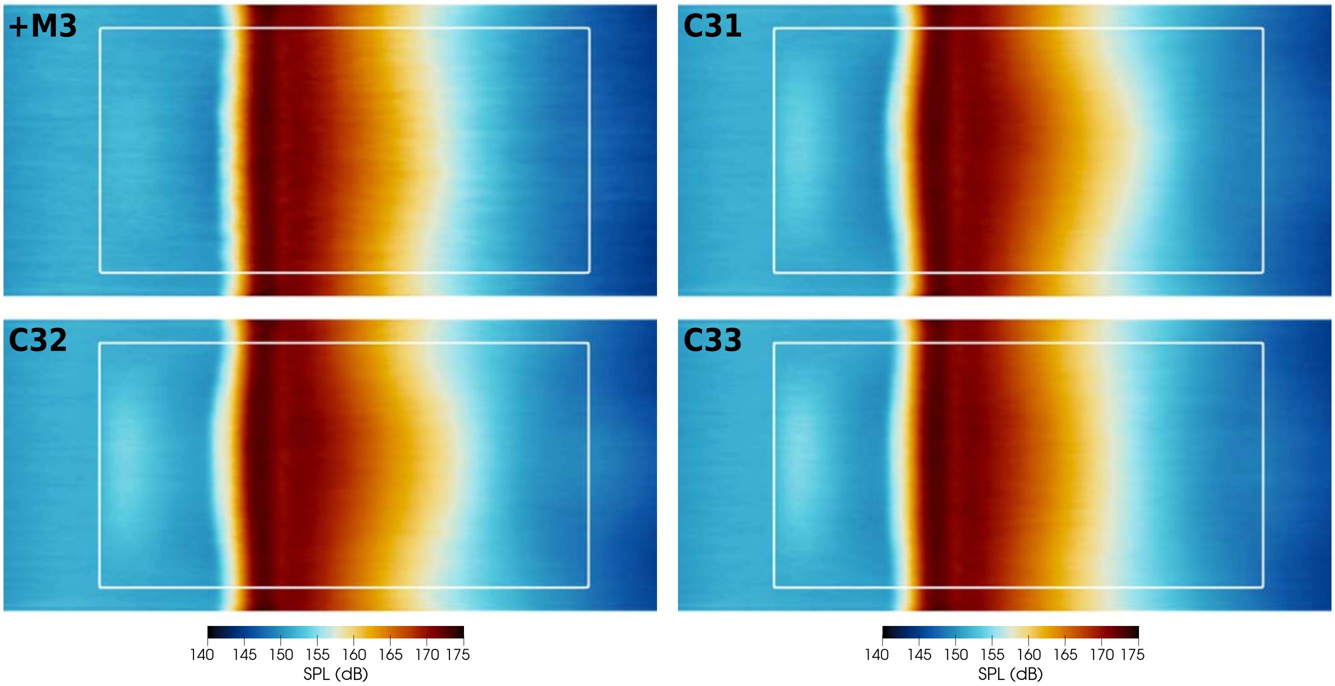

FIG. 27. Sound pressure level (SPL) in decibels (dB) at the surface of the compliant panel indicated by the rectangular region enclosed within the white solid line; +*M*3 static and unsteady deformation modes.

imposed unsteady surface deformations contain several other modes, the turbulent flow pressure appears to react the most to the first mode in the 200-400 Hz frequency range.

The locally strongest low-frequency pressure response is obtained for the case *C*32. The first peak at the SBLI occurs at ~350 Hz and can be observed to extend upstream and downstream. Prior to the 3 kHz peak, there are another couple of frequencies that the pressure responds to, namely at 650 Hz and 850 Hz. These can also be observed to run across most of the panel length, albeit at a weaker response than for the 350 Hz frequency. For case *C*31, the first peak at the SBLI is obtained just below 400 Hz and can also be observed to run across most of the panel length. A secondary peak occurs at around 900 Hz, which appears to cause an even greater response near the compliant panel than the first frequency mode. Of the three unsteady cases, case *C*33 appears to show the

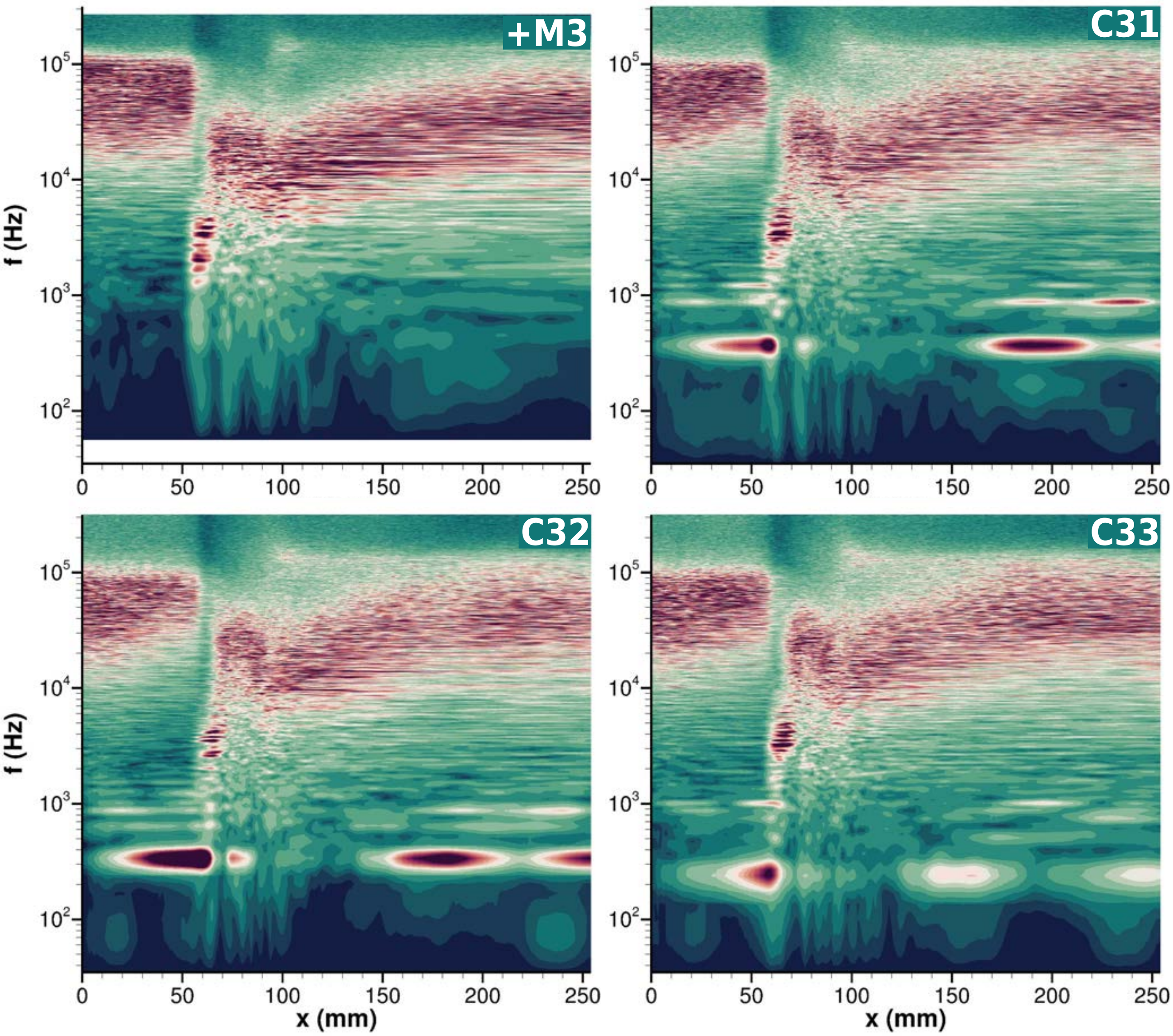

FIG. 28. Spectrogram of the normalized pre-multiplied pressure power-spectrum, $\Phi_n = f\mathcal{P}(x,f)/\int \mathcal{P}(x,f)\,\mathrm{d}f$, along the compliant panel midspan.

least response overall, particularly in the region downstream of the SBLI, though this may be misleading, as will be explained in the next paragraph. The first peak associated with the low-frequency motion of the separated shock at the SBLI occurs at just above 250 Hz. Though many other secondary peaks can be observed before the 3 kHz peak, a small but still noticeable secondary peak occurs at ∼1 kHz, which can also be observed to run across most of the panel length.

A side-effect of the pre-multiplied power spectrum is the multiplication of the power spectrum, $\mathcal{P}$, by its frequency f. As discussed above, the first modal peak occurs at different frequencies between the three vibrating panel cases. So, though case $C33$ appears to show the lowest –local– response, this is only caused by its multiplication by a lower frequency value, e.g., 250 Hz for case $C33$ vs ∼400 Hz for $C31$. Figure 29 demonstrates that in absolute terms, $C33$, in fact, attains the strongest response. Moreover, Fig. 29 reveals a distinct increase in the turbulent flow pressure unsteadiness at an even lower frequency of ∼70 Hz for all three vibrating panel cases. Though weaker than the primary low-frequency mode, it can still be found at different sections along the panel.

Finally, the low-frequency mode that is established in the 1–4 kHz frequency range shows no significant side effects from the panel unsteadiness. However, simulations with a finer mesh resolution at the SBLI would be required to draw a more conclusive argument. Except for the distinct high-frequency pressure oscillation, which occurs just over 100 kHz and is located at the re-attachment of the separation bubble formed by the SBLI, the near wall turbulent flow pressure power-spectrum properties above frequencies of 1 kHz show no sig-

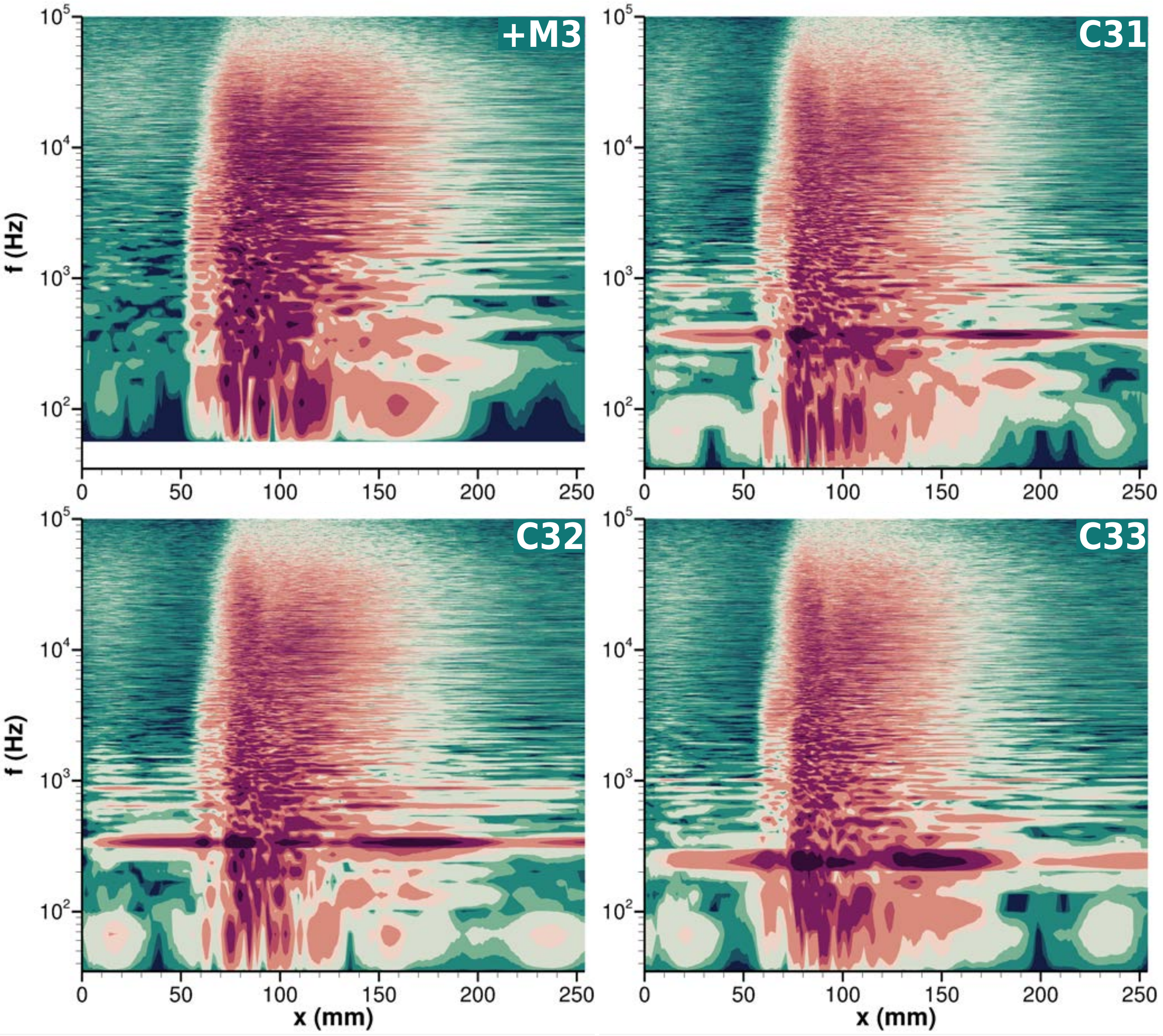

FIG. 29. Spectrogram of the pressure power-spectrum, $\mathcal{P}(x,f)$, in the streamwise ($x-$) direction along the compliant panel midspan; frequency (y-axis) in log-scale for $f \in [0.1,\, 100]$ kHz; $\mathcal{P}$ in units of Pa^2.

nificant response to either the static or vibrating buckled panel cases that were examined.

VII. CONCLUSIONS

Several conclusions can be drawn from this project concerning the computational accuracy of hypersonic flows and acoustics.

ILES can produce highly accurate flow and acoustic metrics results even though a 50 times reduced mesh resolution compared to DNS. It slightly under-predicts the transition peak and delays the transition. However, ILES predicts the correct spectrum roll-off for transitional and turbulent hypersonic boundary layers. Since the ILES captures the near-wall acoustic spectrum roll-off at low/medium frequencies, it would be appropriate for modeling structural dynamic loading.

We examined the performance of the WENO implementation. We showed that implementing a *"normalization"* technique of the WENO candidate stencils further reduces the numerical dissipation of the scheme and thus improves the accuracy of the results, particularly for under-resolved grids. The stencil spans many local surrounding flowfields for high-order numerical schemes, such as the 11^{th}-order WENO. The stencil extent is further exaggerated on a coarser mesh; consequently, the values can differ more significantly. Normalizing the stencil values with a positive real number range also prevents negative value smoothness indicators. In the case of only small jumps across the stencils relative to the minimum absolute value, subtracting the latter ensures the former is sufficiently amplified and "identified" by the smoothness indicators.

For the case of SBLI, the scheme's order significantly affects the accuracy of the DNS and ILES results obtained. High-order methods can resolve smaller turbulent structures in the flow. Consequently, the energy entering the turbulent cascade process at the inertial scale can be distributed across a broader turbulence kinetic energy spectrum range. The higher energy content at the resolved (large) scales in lower-order schemes causes the recirculation bubble to shift further downstream, in contrast to the experimental and numerical (DNS) data. Using low-Mach corrections in the subsonic region of the TBL and recirculation bubble has a negligible effect on the accuracy of the low-order schemes. The above result suggests that supersonic TBL and SBLI are primarily dominated by the processes and resolved turbulence in the supersonic regions of the flow, at least for the conditions considered for the supersonic ramp.

We demonstrated that using high-order, high-resolution methods and reasonably fine grids, ILES provides accurate estimations of several key flow metrics, which are in good agreement with reference DNS data and experimental measurements. In the supersonic ramp case, we believe that the low-frequency oscillation exhibited by the shockwave likely occurs due to the interchange between the foot of the λ-shockwave and the reattachment region of the detached free-shear (mixing) layer. The incoming undisturbed TBL gradually pushes the recirculation bubble downstream and, with it, the shockwave. The above flow development causes the detached shear layer to impinge onto the ramp sooner, steadily raising the pressure close to the ramp corner. The pressure rise travels upstream via the subsonic region of the TBL and separation bubble and eventually becomes sufficiently large to "push" the λ-shock foot back upstream again. The time taken for an acoustic (pressure) wave to travel back and forth, the distance below the sonic line, corresponds closely to that of the low-frequency motion of the shockwave. Then, as the pressure relaxes, the process is repeated, leading to the low-frequency oscillation of the oblique shock observed in SBLI.

We found that the acoustic spectra scaling at Mach 6 differs from incompressible flow across frequencies. Therefore, incompressible models should not be used in high-speed flows. The proposed wall-pressure spectra model COMPRA-G, which includes compressibility effects, gives good estimates of the low and medium frequency regimes based only on freestream properties. This makes its implementation extremely straightforward and fast, avoiding the need for costly computer simulations.

The DNS data of supersonic flow over a compression ramp were analyzed using the CVE method. The flow was decomposed into coherent and incoherent parts by thresholding the wavelet coefficients. The few wavelet coefficients are sufficient to represent the flow's coherent structures that carry most of the flow energy. The PDFs of the vorticity components are skewed for the coherent parts and total fields, and they are perfectly superimposed, showing that the coherent vorticity field preserves the flow statistics.

The PDFs of the incoherent components were found symmetric for all vorticity components for the whole flow. The incoherent part of vorticity appears without an apparent topological structure and low amplitude. However, the analysis shows a correlation between the wall-pressure fluctuations and the incoherent part of vorticity at different positions from the wall. The highest correlation is found in the flow Region III, at $y^+ \simeq 4.3$ ($y = 0.005\delta_0$), for the streamwise and wall-normal vorticity components. Our idea regarding a potential correlation of the pressure fluctuations P and the incoherent vorticity $|\omega|_{\text{inc}}$ is highly speculative. Although the results are not conclusive about the exact nature of this relationship, they show a correlation, which indicates that the incoherent vorticity component carries physical information related to pressure fluctuations, thus to near-wall acoustics. Furthermore, we speculate that the thermodynamic properties of the wall would affect this relationship. If a further investigation proves the above true, we could recover from the velocity field, the incoherent vorticity, and the sound properties of the field. The above are topics of future research.

We assessed the accuracy of different computational models for the RC-19 cases. The RANS method does not accurately predict the maximum value around the SBLI area of the compliant panel. Moreover, the results revealed that the DES approach is unsuitable for the present case. ILES showed promising results even on a coarse mesh examined.

In respect of the SBLI over the compliant panel, the size of the resolved separation/recirculation bubble is found to be greatly affected by the mesh resolution. The results suggest that to resolve the low-frequency shock breathing motion more accurately, coarse-grain ILES should utilize a finer mesh resolution in the area of the SBLI, at least in the streamwise and spanwise directions.

It was found that along the compliant panel midspan, where the maximum deformation amplitude is located, the mean and root-mean-square (RMS) pressure are affected by about 10 per cent compared to the planar (non-deformed) panel case. Despite the weak response of the mean pressure amplitude, the surface contour plots reveal that the streamwise, particularly the spanwise distribution, is mostly affected. The surface deformation modes are shown to disrupt the spanwise constant mean pressure, forming higher (or lower) values at either the panel's midspan or edges, depending on the mode.

The surface curvature leads to a characteristic bending of the spanwise distribution, which can be concave or convex depending on the deformation mode. A buckled panel undergoing a sequence of the examined deformation modes will, thus, be subjected to an altering pressure load distribution, in addition to the mean $\sim$10% variation in pressure amplitude. The results suggest that the deformation rate plays just as important a role as the deformation amplitude in the TBL and SBLI responses. For example, despite the amplitude of mode 3 being almost a quarter of mode 1, the overall response – at least for the flow properties investigated– was equivalent. Therefore, the increased deformation rate of the mode 3-panel surface can only be reasoned.

The six cases for static deformation showed that the spanwise location of the peak pressure varies depending on the deformation mode. A power-spectrum analysis of the pressure fluctuation at and post the SBLI along the mid-span of the compliant panel showed that the pressure power spectra magnitude at the low-frequency range, $f \in [100, 1,000]$ Hz, changes 6-7 times between modes -M2 (lowest) and +M3 (highest) particularly at the SBLI. The RC-19 cases are in progress, and a detailed report will be produced soon.

The vibrating panel cases introduce additional low-frequency modes in the pressure power spectrum that were not previously observed. The enhancement occurs from as low as $\sim$70 Hz, while strongest at the range of 250–400 Hz. Typically, said three modes persist across most of the compliant panel's length. Above 1 kHz, the turbulent flow's near-wall pressure power-spectrum properties show little to no response to the compliant panel surface deformation for either the static or vibrating cases presently examined.

VIII. ACKNOWLEDGMENTS

This material is based upon work supported by the Air Force Office of Scientific Research under award numbers FA9550-19-1-7018. DD thanks Dr David Swanson (Air Force Office of Scientific Research - European Office of Aerospace) for his support. The funding was awarded to DD through the University of Nicosia Research Foundation.

REFERENCES

[1] Z. B. Riley, R. A. Perez, G. W. Bartram, S. M. Spottswood, B. P. Smarslok, and T. J. Beberniss, "Aerothermoelastic experimental design for the AEDC/VKF Tunnel C: Challenges associated with measuring the response of flexible panels in high-temperature, high-speed wind tunnels," Journal of Sound and Vibration **441**, 96 – 105 (2019).

[2] S. M. Spottswood, T. J. Beberniss, T. G. Eason, R. A. Perez, J. M. Donbar, D. A. Ehrhardt, and Z. B. Riley, "Exploring the response of a thin, flexible panel to shock-turbulent boundary-layer interactions," Journal of Sound and Vibration **443**, 74 – 89 (2019).

[3] J. Poggie and K. M. Porter, "Flow structure and unsteadiness in a highly confined shock-wave–boundary-layer interaction," Phys. Rev. Fluids **4**, 024602 (2019).

[4] K. M. Porter and J. Poggie, "Selective upstream influence on the unsteadiness of a separated turbulent compression ramp flow," Physics of Fluids **31**, 016104 (2019).

[5] I. Kokkinakis, D. Drikakis, K. Ritos, and S. M. Spottswood, "Direct numerical simulation of supersonic flow and acoustics over a compression ramp," Physics of Fluids **32**, 066107 (2020).

[6] K. Ritos, D. Drikakis, , I. W. Kokkinakis, and S. M. Spottswood, "Computational aeroacoustics beneath high speed transitional and turbulent boundary layers," Computers and Fluids **203**, 104520 (2020).

[7] A. Ceci, A. Palumbo, J. Larsson, and S. Pirozzoli, "On low-frequency unsteadiness in swept shock wave–boundary layer interactions," Journal of Fluid Mechanics **956**, R1 (2023).

[8] C. Jenquin, E. C. Johnson, and V. Narayanaswamy, "Investigations of shock–boundary layer interaction dynamics using high-bandwidth pressure field imaging," Journal of Fluid Mechanics **961**, A5 (2023).

[9] K. Ritos, I. W. Kokkinakis, and D. Drikakis, "Physical insight into the accuracy of finely-resolved iLES in turbulent boundary layers," Computers & Fluids **169**, 309 – 316 (2018).

[10] D. Drikakis, K. Ritos, S. M. Spottswood, and Z. B. Riley, "Flow transition to turbulence and induced acoustics at mach 6," Physics of Fluids **33**, 076112 (2021).

[11] N. T. Clemens and V. Narayanaswamy, "Low-frequency unsteadiness of shock wave/turbulent boundary layer interactions," Annual Review of Fluid Mechanics **46**, 469–492 (2014).

[12] J. Délery and J.-P. Dussauge, "Some physical aspects of shock wave/boundary layer interactions," Shock Waves **19**, 453–468 (2009).

[13] P. L. Ardonceau, "The structure of turbulence in a supersonic shock-wave/boundary-layer interaction," AIAA Journal **22**, 1254–1262 (1984).

[14] D. S. Dolling and C. T. Or, "Unsteadiness of the shock wave structure in attached and separated compression ramp flows," Experiments in Fluids **3**, 24 – 32 (1985).

[15] A. J. Smits and K.-C. Muck, "Experimental study of three shock wave/turbulent boundary layer interactions," Journal of Fluid Mechanics **182**, 291–314 (1987).

[16] S. J. Beresh, N. T. Clemens, and D. S. Dolling, "Relationship between upstream turbulent boundary-layer velocity fluctuations and separation shock unsteadiness," AIAA Journal **40**, 2412–2422 (2002).

[17] P. Bookey, C. Wyckham, A. Smits, and P. Martin, "New experimental data of STBLI at DNS/LES accessible Reynolds numbers," in *43rd AIAA Aerospace Sciences Meeting and Exhibit* (American Institute of Aeronautics and Astronautics, Reno, Nevada, 2005).

[18] B. Ganapathisubramani, N. T. Clemens, and D. S. Dolling, "Low-frequency dynamics of shock-induced separation in a compression ramp interaction," Journal of Fluid Mechanics **636**, 397–425 (2009).

[19] Z. B. Riley, R. A. Pereza, G. W. Bartrama, S. M. Spottswood, B. P. Smarslok, and T. J. Beberniss, "Aerothermoelastic experimental design for the aedc/vkf tunnel c: Challenges associated with measuring the response of flexible panels in high-temperature, high-speed wind tunnels," Journal of Sound and Vibration **441**, 96–105 (2019).

[20] G. S. Settles, T. J. Fitzpatrick, and S. M. Bogdonoff, "Detailed study of attached and separated compression corner flowfields in high Reynolds number supersonic flow," AIAA Journal **17**, 579–585 (1979).

[21] D. S. Dolling and M. E. Erengil, "Unsteady wave structure near separation in a Mach 5 compression ramp interaction," AIAA Journal **29**, 728–735 (1991).

[22] N. A. Adams, "Direct simulation of the turbulent boundary layer along a compression ramp at $M = 3$ and $Re_\theta = 1685$," Journal of Fluid Mechanics **420**, 47–83 (2000).

[23] D. P. Rizzetta and M. R. Visbal, "Application of large-eddy simulation to supersonic compression ramps," AIAA Journal **40**, 1574–1581 (2002).

[24] M. Wu and M. P. Martin, "Direct numerical simulation of supersonic turbulent boundary layer over a compression ramp," AIAA Journal **45**, 879 – 889 (2007).

[25] M. Wu and M. P. Martín, "Analysis of shock motion in shockwave and turbulent boundary layer interaction using direct numerical simulation data," Journal of Fluid Mechanics **594**, 71–83 (2008).

[26] E. Touber and N. D. Sandham, "Large-eddy simulation of low-frequency unsteadiness in a turbulent shock-induced separation bubble," Theoretical and Computational Fluid Dynamics **23**, 79 – 107 (2009).

[27] X. Li, D. Fu, Y. Ma, and X. Liang, "Direct numerical simulation of shock/turbulent boundary layer interaction in a supersonic compression ramp," Science China Physics, Mechanics and Astronomy **53**, 1651 – 1658 (2010).

[28] S. Priebe and M. P. Martín, "Low-frequency unsteadiness in shock wave-turbulent boundary layer interaction," Journal of Fluid Mechanics **699**, 1–49 (2012).

[29] B. Morgan, K. Duraisamy, N. Nguyen, S. Kawai, and S. K. Lele, "Flow physics and RANS modelling of oblique shock/turbulent boundary layer interaction," Journal of Fluid Mechanics **729**, 231–284 (2013).

[30] S. Priebe, J. H. Tu, C. W. Rowley, and M. P. Martín, "Low-frequency dynamics in a shock-induced separated flow," Journal of Fluid Mechanics **807**, 441–477 (2016).

[31] M. P. Martin, S. Priebe, and C. M. Helm, "Upstream and downstream influence on STBLI instability," in *46th AIAA Fluid Dynamics Conference* (American Institute of Aeronautics and Astronautics, 2016).

[32] F. Tong, C. Yu, Z. Tang, and X. Li, "Numerical studies of shock wave interactions with a supersonic turbulent boundary layer in compression corner: Turning angle effects," Computers & Fluids **149**, 56 – 69 (2017).

[33] K. M. Porter and J. Poggie, "Turbulence structure and large-scale unsteadiness in shock-wave / boundary layer interaction," in *55th AIAA Aerospace Sciences Meeting* (American Institute of Aeronautics and Astronautics,

2017).

[34] S. M. Spottswood, T. Eason, and T. Beberniss, "Influence of shock-boundary layer interactions on the dynamic response of a flexible panel," Proceedings of the ISMA-2012 , 17–19 (2012).

[35] M. Visbal, "On the interaction of an oblique shock with a flexible panel," Journal of Fluids and Structures **30**, 219–225 (2012).

[36] B. A. Miller, A. R. Crowell, R. Deshmukh, A. Gogulapati, J. J. McNamara, V. Vyas, X. Wang, and M. P. Mignolet, "Response of a panel to shock impingement: Modeling and comparison with experiments," in *55th AIAA/ASME/ASCE/AHS/ASC Structures, Structural Dynamics, and Materials Conference* (2014).

[37] R. Wiebe and S.M.Spottswood, "On the dimension of complex responses in nonlinear structural vibrations," Journal of Sound and Vibration **373**, 192–204 (2016).

[38] K. R. Brouwer, A. Gogulapati, and J. J. McNamara, "Interplay of surface deformation and shock-induced separation in shock/boundary-layer interactions," AIAA Journal **55**, 4258–4273 (2017).

[39] S. M. Spottswood, T. J. Beberniss, T. G. Eason, R. A. Perez, J. M. Donbar, D. A. Ehrhardt, and Z. B. Riley, "Exploring the response of a thin, flexible panel to shock-turbulent boundary-layer interactions," Journal of Sound and Vibration **443**, 74 – 89 (2019).

[40] M. C. Neet and J. M. Austin, "Effects of surface compliance on shock boundary layer interaction in the caltech mach 4 ludwieg tube," in *AIAA Scitech 2020 Forum*.

[41] T. J. Whalen, A. G. Schöneich, S. J. Laurence, B. T. Sullivan, D. J. Bodony, M. Freydin, E. H. Dowell, and G. M. Buck, "Hypersonic fluid–structure interactions in compression corner shock-wave/boundary-layer interaction," AIAA Journal **58**, 4090–4105 (2020).

[42] D. Daub, B. Esser, and A. Gülhan, "Experiments on high-temperature hypersonic fluid–structure interaction with plastic deformation," AIAA Journal **58**, 1423–1431 (2020).

[43] A. Tripathi, J. Gustavsson, K. Shoele, and R. Kumar, "Response of a compliant panel to shock boundary layer interaction at mach 2," in *AIAA Scitech 2021 Forum*.

[44] K. R. Brouwer, R. A. Perez, T. J. Beberniss, S. M. Spottswood, and D. A. Ehrhardt, "Experiments on a thin panel excited by turbulent flow and shock/boundary-layer interactions," AIAA Journal **59**, 2737–2752 (2021).

[45] K. R. Brouwer, R. A. Perez, T. J. Beberniss, S. M. Spottswood, and D. A. Ehrhardt, "Evaluation of reduced-order aeroelastic simulations for shock-dominated flows," Journal of Fluids and Structures **108**, 103429 (2022).

[46] K. R. Brouwer, R. Perez, T. J. Beberniss, and S. M. Spottswood, "Aeroelastic experiments and companion computations assessing the impact of impinging shock sweep," in *AIAA SCITECH 2023 Forum*.

[47] K. R. Brouwer, R. Perez, T. J. Beberniss, and S. M. Spottswood, "Surface pressure measurements and predictions in shock-dominated flows," in *AIAA AVIATION 2023 Forum*.

[48] S. J. Peltier, K. R. Brouwer, R. Perez, S. M. Spottswood, and S. Hammack, "Boundary-layer measurements for ftsi systems: Influence of panel flutter on a mach 2 turbulent boundary-layer," in *AIAA SCITECH 2023 Forum*.

[49] A. D'Aguanno, P. Quesada Allerhand, F. F. J. Schrijer, and B. W. van Oudheusden, "Characterization of shock-induced panel flutter with simultaneous use of dic and piv," Experiments in Fluids **64** (2023), 10.1007/s00348-022-03551-1.

[50] M. Visbal, "Viscous and inviscid interactions of an oblique shock with a flexible panel," Journal of Fluids and Structures **48**, 27–45 (2014).

[51] N. R. Boyer, J. McNamara, D. Gaitonde, C. J. Barnes, and M. R. Visbal, "Features of shock-induced panel flutter in three-dimensional inviscid flow," Journal of Fluids and Structures **83**, 490–506 (2018).

[52] Y. Li, H. Luo, X. Chen, and J. Xu, "Laminar boundary layer separation over a fluttering panel induced by an oblique shock wave," Journal of Fluids and Structures **90**, 90–109 (2019).

[53] N. R. Boyer, J. McNamara, D. Gaitonde, C. J. Barnes, and M. R. Visbal, "Features of panel flutter response to shock boundary layer interactions," Journal of Fluids and Structures **101**, 103207 (2021).

[54] V. Shinde, A. Becks, R. Deshmukh, J. McNamara, D. Gaitonde, M. Neet, and J. Austin, "Spatially developing supersonic turbulent boundary layer subjected to static surface deformations," European Journal of Mechanics - B/Fluids **89**, 485–500 (2021).

[55] J. F. Hoy and I. Bermejo-Moreno, "Numerical study of stbli on flexible panels with wall-modeled les," in *AIAA Scitech 2021 Forum*.

[56] A. Zope, C. Horner, E. M. Collins, S. Bhushan, and M. Bhatia, "Investigation of flexible panel dynamic response induced by coherent turbulent vortical structures," in *AIAA Scitech 2021 Forum*.

[57] K. R. Brouwer, R. A. Perez, T. J. Beberniss, S. M. Spottswood, D. A. Ehrhardt, and R. Wiebe, "Investigation of aeroelastic instabilities for a thin panel in turbulent flow," Nonlinear Dynamics **104**, 3323–3346 (2021).

[58] J. D. Thayer, J. J. McNamara, and D. V. Gaitonde, "Unsteady aerodynamic response of a high-speed, separated flow to a deforming cantilever plate," in *AIAA SCITECH 2022 Forum*.

[59] V. Shinde, J. McNamara, and D. Gaitonde, "Dynamic interaction between shock wave turbulent boundary layer and flexible panel," Journal of Fluids and Structures **113**, 103660 (2022).

[60] F. F. Grinstein, ed., *Coarse Grained Simulation and Turbulent Mixing* (Cambridge University Press, 2016).

[61] W. K. George and M. Tutkun, "Mind the gap: A guideline for large eddy simulation," Philosophical Transactions: Mathematical, Physical and Engineering Sciences **367**, 2839–2847 (2009).

[62] K. Ritos, I. W. Kokkinakis, D. Drikakis, and S. M. Spottswood, "Implicit large eddy simulation of acoustic loading in supersonic turbulent boundary layers," Physics of Fluids **29**, 046101 (2017).

[63] K. Ritos, D. Drikakis, and I. Kokkinakis, "Acoustic loading beneath hypersonic transitional and turbulent boundary layers," Journal of Sound and Vibration **441**, 50 – 62 (2019).

[64] I. W. Kokkinakis and D. Drikakis, "Near-wall behaviour of implicit large eddy simulations," in *ECCOMAS Congress 2016 - Proceedings of the 7th European Congress on Computational Methods in Applied Sciences and Engineering*, Vol. 1 (National Technical University of Athens, 2016) pp. 1032–1045.

[65] K. Ritos, I. W. Kokkinakis, and D. Drikakis, "Physical insight into a mach 7.2 compression corner flow," in *2018 AIAA Aerospace Sciences Meeting* (2018).

[66] G. Khujadze, K. Ritos, I. Kokkinakis, D. Drikakis, and S. Spottswood, "Wavelet analysis of high-speed transition and turbulence over a flat surface," Physics of Fluids , 046107 (2022).

[67] I. W. Kokkinakis, G. Khujadze, D. Drikakis, and S. M. Spottswood, "Wavelet analysis of supersonic shock-boundary-layer interaction," Physics of Fluids **35**, 066106 (2023), https://pubs.aip.org/aip/pof/article-pdf/doi/10.1063/5.0153863/17937654/066106_1_5.0153863.pdf.

[68] I. W. Kokkinakis, D. Drikakis, S. M. Spottswood, K. R. Brouwer, and Z. B. Riley, "High-speed shock–boundary-layer interaction over deformed surfaces," Physics of Fluids **35**, 106109 (2023), https://pubs.aip.org/aip/pof/article-pdf/doi/10.1063/5.0172475/18174721/106109_1_5.0172475.pdf.

[69] B. Van Leer, "Towards the ultimate conservative difference scheme III. Upstream-centered finite-difference schemes for ideal compressible flow," Journal of Computational Physics **23**, 263 – 275 (1977).

[70] K. H. Kim and C. Kim, "Accurate, efficient and monotonic numerical methods for multi-dimensional compressible flows: Part II: Multi-dimensional limiting process," Journal of Computational Physics **208**, 570 – 615 (2005).

[71] D. S. Balsara and C.-W. Shu, "Monotonicity preserving weighted essentially non-oscillatory schemes with increasingly high order of accuracy," Journal of Computational Physics **160**, 405 – 452 (2000).

[72] R. Spiteri and S. Ruuth, "A new class of optimal high-order strong-stability-preserving time discretization methods," SIAM Journal on Numerical Analysis **40**, 469–491 (2002).

[73] I. Kokkinakis and D. Drikakis, "Implicit large eddy simulation of weakly-compressible turbulent channel flow," Computer Methods in Applied Mechanics and Engineering **287**, 229 – 261 (2015).

[74] P. Tsoutsanis, I. W. Kokkinakis, L. Könözsy, D. Drikakis, R. J. Williams, and D. L. Youngs, "Comparison of structured- and unstructured-grid, compressible and incompressible methods using the vortex pairing problem," Computer Methods in Applied Mechanics and Engineering **293**, 207 – 231 (2015).

[75] B. Thornber, A. Mosedale, D. Drikakis, D. Youngs, and R. Williams, "An improved reconstruction method for compressible flows with low Mach number features," Journal of Computational Physics **227**, 4873 – 4894 (2008).

[76] C. W. Shu, "Numerical experiments on the accuracy of ENO and modified ENO schemes," Journal of Scientific Computing **5**, 127–149 (1990).

[77] X.-D. Liu, S. Osher, and T. Chan, "Weighted essentially non-oscillatory schemes," Journal of Computational Physics **115**, 200 – 212 (1994).

[78] G.-S. Jiang and C.-W. Shu, "Efficient implementation of weighted ENO schemes," Journal of Computational Physics **126**, 202 – 228 (1996).

[79] C.-W. Shu, "Essentially non-oscillatory and weighted essentially non-oscillatory schemes for hyperbolic conservation laws," in *Advanced Numerical Approximation of Nonlinear Hyperbolic Equations: Lectures given at the 2nd Session of the Centro Internazionale Matematico Estivo (C.I.M.E.) held in Cetraro, Italy, June 23–28, 1997*, edited by A. Quarteroni (Springer Berlin Heidelberg, Berlin, Heidelberg, 1998) pp. 325–432.

[80] C. Shu, "High order weighted essentially nonoscillatory schemes for convection dominated problems," SIAM Review **51**, 82–126 (2009).

[81] A. K. Henrick, T. D. Aslam, and J. M. Powers, "Mapped weighted essentially non-oscillatory schemes: Achieving optimal order near critical points," Journal of Computational Physics **207**, 542 – 567 (2005).

[82] E. M. Taylor, M. Wu, and M. P. Martín, "Optimization of nonlinear error for weighted essentially non-oscillatory methods in direct numerical simulations of compressible turbulence," Journal of Computational Physics **223**, 384 – 397 (2007).

[83] O. Zanotti and M. Dumbser, "Efficient conservative ADER schemes based on WENO reconstruction and space-time predictor in primitive variables," Computational Astrophysics and Cosmology **3**, 1–32 (2016).

[84] R. H. Nichols, R. W. Tramel, and P. G. Buning, "Evaluation of two high-order weighted essentially nonoscillatory schemes," AIAA Journal **46**, 3090–3102 (2008).

[85] H. Feng, C. Huang, and R. Wang, "An improved mapped weighted essentially non-oscillatory scheme," Applied Mathematics and Computation **232**, 453 – 468 (2014).

[86] A. Harten, B. Engquist, S. Osher, and S. R. Chakravarthy, "Uniformly high order accurate essentially non-oscillatory schemes, III," Journal of Computational Physics **131**, 3 – 47 (1997).

[87] V. Titarev and E. Toro, "Finite-volume WENO schemes for three-dimensional conservation laws," Journal of Computational Physics **201**, 238 – 260 (2004).

[88] E. F. Toro, M. Spruce, and W. Speares, "Restoration of the contact surface in the HLL-Riemann solver," Shock Waves **4**, 25 – 34 (1994).

[89] E. F. Toro, *Riemann Solvers and Numerical Methods for Fluid Dynamics, A Practical Introduction*, 3rd ed. (Springer-Verlag Berlin Heidelberg, 2009).

[90] E. F. Toro, "A linearized Riemann solver for the time-dependent Euler equations of gas dynamics," Proceedings of the Royal Society of London. Series A: Mathematical and Physical Sciences **434**, 683–693 (1991).

[91] E. F. Toro, "Direct Riemann solvers for the time-dependent Euler equations," Shock Waves **5**, 75 (1995).

[92] S. Davis, "Simplified second-order Godunov-type methods," SIAM Journal on Scientific and Statistical Computing **9**, 445–473 (1988).

[93] X. Wu, J. M. Wallace, and J.-P. Hickey, "Boundary layer turbulence and freestream turbulence interface, turbulent spot and freestream turbulence interface, laminar boundary layer and freestream turbulence interface," Physics of Fluids , 045104 (2019).

[94] J. Blazek, *Fluid Dynamics, Principles and Applications* (Elsevier, 2015).

[95] D. Drikakis, M. Hahn, A. Mosedale, and B. Thornber, "Large eddy simulation using high resolution and high order methods," Proc. R. Soc. A **367**, 2985–2997 (2009).

[96] P. Tsoutsanis, I. W. Kokkinakis, L. Konozsy, D. Drikakis, R. J. R. Williams, and D. L. Youngs, "Comparison of structured and unstructured-grid, compressible and incompressible methods using the vortex pairing problem," Comput. Method. Appl. M. **293**, 207–231 (2015).

[97] D. A. Bies, "A review of flight and wind tunnel measurements of boundary layer pressure fluctuations and induced structural response," Tech. Rep. NASA-CR-626 (NASA, 1965).

[98] X. Zhao and L. Zhao, "Wall pressure fluctuations beneath hypersonic boundary layer over plate," AIAA Journal , 1–10 (2020).

[99] J. Huang, L. Duan, K. Casper, R. Wagnild, and N. Bitter, "Direct numerical simulation of turbulent pressure fluctuations over a cone at Mach 8," in *AIAA SicTech Forum*, AIAA 2020-1065 (2020).

[100] M. Goody, "Empirical spectral model of surface pressure fluctuations," AIAA Journal **42**, 1788–1794 (2004).

[101] K. Ritos, D. Drikakis, and I. W. Kokkinakis, "Wall-pressure spectra models for supersonic and hypersonic turbulent boundary layers," Journal of Sound and Vibration **443**, 90 – 108 (2019).

[102] M. S. Howe, *Acoustics of Fluid-structure Interactions* (Cambridge University Press, 1998).

[103] W. K. Blake, *Mechanics of Flow-Induced Sound and Vibration* (New York: Academic Press, 1986).

[104] M. Bull, "Wall-pressure fluctuations beneath turbulent boundary layers: some reflections on forty years of research," Journal of Sound and Vibration **190**, 299 – 315 (1996).

[105] J. E. Ffowcs-Williams, "Surface pressure fluctuations induced by boundary layer flow at finite Mach number," J. Fluid Mech. **22**, 507–519 (1965).

[106] L. Duan, M. M. Choudhari, and C. Zhang, "Pressure fluctuations induced by a hypersonic turbulent boundary layer," Journal of Fluid Mechanics **804**, 578–607 (2016).

[107] C. Zhang, L. Duan, and M. M. Choudhari, "Effect of wall cooling on boundary-layer-induced pressure fluctuations at mach 6," J. Fluid Mech. **822**, 5–30 (2017).

[108] S. J. Beresh, J. F. Henfling, R. W. Spillers, and B. O. M. Pruett, "Fluctuating wall pressures measured beneath a supersonic turbulent boundary layer," Phys. Fluids **23**, 1–16 (2011).

[109] M. Bernardini, S. Pirozzoli, and F. Grasso, "The wall pressure signature of transonic shock/boundary layer interaction," Journal of Fluid Mechanics **671**, 288–312 (2011).

[110] R. H. Kraichnan, "Pressure fluctuations in turbulent flow over a flat plate," J. Acoust. Soc. Am. **28**, 378–390 (1956).

[111] O. M. Phillips, "On the aerodynamic surface sound from a plane turbulent boundary," Proc. R. Soc. A **234**, 327–335 (1956).

[112] P. Bradshaw, "Inactive motion and pressure fluctuations in turbulent boundary layers," J. Fluid Mech. **30**, 241–258 (1967).

[113] R. L. Panton and J. H. Linebarger, "Wall pressure spectra calculations for equilibrium boundary layers," J. Fluid Mech. **65**, 261–287 (1974).

[114] S. P. Gravante, A. M. Naguip, C. E. Wark, and H. M. Nagib, "Characterization of the pressure fluctuations under a fully developed turbulent boundary layer," AIAA Journal **36**, 1808–1816 (1998).

[115] G. K. Batchelor, "Pressure fluctuations in isotropic turbulence," Proc. Camb. Phil. Soc. **47**, 359–374 (1951).

[116] G. Schewe, "On the Structure and Resolution of Wall-Pressure Fluctuations Associated with Turbulent Boundary Layer Flow," J. Fluid Mech. **134**, 311–328 (1983).

[117] Y. Tsuji and T. Ishihara, "Similarity scaling of pressure fluctuation in turbulence," Phys. Rev. E **68**, 026309 (2003).

[118] R. Camussi, M. felli, F. Pereira, G. Aloisio, and A. D. Marco, "Statistical properties of wall pressure fluctuations over a forward-facing step," Phys. Fluids **20**, 075113 (2008).

[119] T. M. Farabee and M. J. Casarella, "Spectral features of wall pressure fluctuations beneath turbulent boundary layers," Phys. Fluids A **3**, 2410–2420 (1991).

[120] D. Drikakis, "Hypersonic acoustic loading," Tech. Rep. Year 1, Award FA9550-19-1-7018 (University of Nicosia, Nicosia, Cyprus, 2020).

[121] D. Drikakis, "Hypersonic acoustic loading," Tech. Rep. Year 1, Award FA9550-19-1-7018 (University of Nicosia, Nicosia, Cyprus, 2021).

[122] K. Ritos, I. W. Kokkinakis, and D. Drikakis, "Performance of high–order implicit large eddy simulations," Computers & Fluids **173**, 307 – 312 (2018).

[123] K. Ritos, D. Drikakis, and I. Kokkinakis, "Acoustic loading beneath hypersonic transitional and turbulent boundary layers," Journal of Sound and Vibration **441**, 50 – 62 (2019).

[124] V. Kolář, "Compressibility effect in vortex identification," AIAA Journal **47**, 473–475 (2009).

[125] V. Kolář and J. Šístek, "Corotational and compressibility aspects leading to a modification of the vortex-identification Q-criterion," AIAA Journal **53**, 2406–2410 (2015).

[126] D. Drikakis, "Hypersonic acoustic loading," Tech. Rep. Year 1, Award FA9550-19-1-7018 (University of Nicosia, Nicosia, Cyprus, 2022).

[127] M. Morkovin, "Effects of compressibility on turbulent flows," in *The Oxford Handbook of Innovation*, edited by A. Favre (Gordon and Breach, New York, 1962) pp. 367–380.

[128] P. Bradshaw, "Compressible turbulent shear layers," Annual Review of Fluid Mechanics **9**, 33–52 (1977).

[129] W. Shyy and V. Krishnamurty, "Compressibility effects in modeling complex turbulent flows," Progress in Aerospace Sciences **33**, 587–645 (1997).

[130] N. J. Georgiadis, D. P. Rizzetta, and C. Fureby, "Large-eddy simulation: current capabilities, recommended practices, and future research." AIAA Journal **48**, 1172–1784 (2010).

[131] H. Choi and P. Moin, "Grid-point requirements for large eddy simulation: Chapman's estimates revisited," Physics of Fluids **24**, 011702 (2012).

[132] J. Poggie, N. J. Bisek, and R. Gosse, "Resolution effects in compressible, turbulent boundary layer simulations," Computers & Fluids **120**, 57–69 (2015).

[133] M. Frigo and S. Johnson, "The design and implementation of fftw3," Proceedings of the IEEE **93**, 216–231 (2005).

[134] M. Bernardini, G. Della Posta, F. Salvadore, and E. Martelli, "Unsteadiness characterisation of shock wave/turbulent boundary-layer interaction at moderate Reynolds number," Journal of Fluid Mechanics **954**, A43 (2023).

[135] P. Dupont, C. Haddad, and J. F. Debiève, "Space and time organization in a shock-induced separated boundary layer," Journal of Fluid Mechanics **559**, 255–277 (2006).

[136] M. Grilli, P. J. Schmid, S. Hickel, and N. A. Adams, "Analysis of unsteady behaviour in shockwave turbulent boundary layer interaction," Journal of Fluid Mechanics **700**, 16–28 (2012).

[137] V. Pasquariello, S. Hickel, N. Adams, G. Hammerl, W. Wall, D. Daub, S. Willems, and A. Gülhan, "Coupled simulation of shock-wave/turbulent boundary-layer interaction over a flexible panel," (6th European Conference for Aeronautics and Space Sciences, 2015).